

A NEW CODE FOR PROTO-NEUTRON STAR EVOLUTION

L. F. ROBERTS[†]Department of Astronomy and Astrophysics, University of California, Santa Cruz, California 95064, USA
Draft version February 25, 2024

ABSTRACT

A new code for following the evolution and emissions of proto-neutron stars during the first minute of their lives is developed and tested. The code is one dimensional, fully implicit, and general relativistic. Multi-group, multi-flavor neutrino transport is incorporated that makes use of variable Eddington factors obtained from a formal solution of the static general relativistic Boltzmann equation with linearized scattering terms. The timescales of neutrino emission and spectral evolution obtained using the new code are broadly consistent with previous results. Unlike other recent calculations, however, the new code predicts that the neutrino-driven wind will be characterized, at least for part of its existence, by a neutron excess. This change, potentially consequential for nucleosynthesis in the wind, is due to an improved treatment of the charged-current interactions of electron flavored neutrinos and anti-neutrinos with nucleons. A comparison is also made between the results obtained using either variable Eddington factors or simple equilibrium flux-limited diffusion. The latter approximation, which has been frequently used in previous studies of proto-neutron star cooling, accurately describes the total neutrino luminosities (to within 10%) for most of the evolution, until the proto-neutron star becomes optically thin.

1. INTRODUCTION

A proto-neutron star (PNS) is born after the core of a massive star collapses to supra-nuclear densities, experiences core bounce due to the repulsive portion of the nuclear interaction which launches a shock wave that may eventually serve to disrupt the entire star in a supernova, and leaves behind a compact remnant. The overlying star is ejected and some portion of the mass may or may not fall back (c.f. Janka et al. 2007). In reality the mass of the PNS may increase with time due to this accretion, but a frequent assumption that is reasonable for low mass progenitors, and one adopted here, is that the PNS evolves in isolation after the shock has exited. Because of the large release of gravitational binding energy ($2 - 5 \times 10^{53}$ ergs), the PNS is initially hot and extended compared to a cold neutron star but large portions of the mass are still at supra-nuclear densities. Due to the high density and reasonably large temperature of this nuclear material, it is opaque to neutrinos of all flavors. In the outer regions of the PNS where the density is lower, the material is semi-transparent to neutrinos. This hot extended object undergoes Kelvin-Helmholtz cooling by emitting neutrinos of all flavors over a period of up to a minute (Burrows & Lattimer 1986), at which time it transitions to a phase of optically thin neutrino cooling.

This qualitative description was confirmed when about twenty neutrinos were observed from SN 1987A (Bionta et al. 1987; Hirata et al. 1987). There were not enough events, however, to determine much detail of the cooling process (Lattimer & Yahil 1989; Loredano & Lamb 2002), though limits were placed on the properties of weakly interacting particles (Keil et al. 1997). If a similar core collapse supernova were to occur today, modern neutrino detectors would see thousands of events. Detailed modeling of the neutrino emission is needed if we are to learn about the central engine of core collapse su-

pernovae from a nearby event.

There are numerous other reasons why understanding the properties of late-time supernova neutrinos is important, despite the rarity with which they are *directly* detected. An important one is the impact of neutrinos on supernova nucleosynthesis. Charged current neutrino interactions in the wind blown from the surface of PNSs determine the electron fraction of the ejected material and thereby constrain its nucleosynthesis. Current uncertainties in the relative energies of the electron neutrinos and anti-neutrinos are large enough to allow for both neutron-rich and proton-rich ejecta, which may be favorable for *r*-process (Woosley et al. 1994) and *νp* -process nucleosynthesis (Fröhlich et al. 2006; Pruet et al. 2006), respectively. Recent work points to the wind ejecta being proton rich at all times (Hüdepohl et al. 2010; Fischer et al. 2010), but the reasons for this change are only beginning to be understood (Fischer et al. 2011). Additionally, the average energies of μ and τ neutrinos also significantly affect the neutrino spallation rates that determine nucleosynthetic yields of the ν -process (Woosley et al. 1990), which may be responsible for a number of rare isotopes.

It is also possible that current neutrino detectors with upgrades or next generation neutrino detectors will be able to observe the diffuse background of neutrinos produced by supernovae over the lifetime of the universe (Horiuchi et al. 2009). Predictions for the diffuse MeV scale neutrino background density depend significantly on the integrated spectrum of neutrinos emitted in core-collapse supernovae (Woosley et al. 1986; Ando 2004). The integrated neutrino emission is dominated by PNS evolution, so that accurate modeling of PNSs can contribute to understanding the diffuse supernova neutrino background.

Finally, the neutrino emission from the “photosphere” of PNSs gives the initial conditions for the study of both matter-induced and neutrino-induced neutrino oscillations (Duan et al. 2006). The differences between the

[†]lroberts@ucolick.org

spectra of various neutrino flavors, especially $\bar{\nu}_e$ and $\bar{\nu}_{\mu,\tau}$, can significantly affect the impact of flavor evolution in the nearly free streaming regime (Keil et al. 2003). The rate of PNS cooling also has the potential to put limits on exotic physics, such as axions (Keil et al. 1995), the presence of quark matter or a Kaon condensate in the core (Pons et al. 2001a,b), as well as possible extensions of the standard model using data already in hand from SN 1987A.

Theoretical predictions of post-bounce neutrinos have existed for more than 25 years (Burrows & Lattimer 1986; Mayle et al. 1987; Keil & Janka 1995; Sumiyoshi et al. 1995; Pons et al. 1999; Fischer et al. 2010; H  depohl et al. 2010; Roberts et al. 2012). Since the evolution of PNSs is described by the Kelvin-Helmholtz cooling of the collapsed, shock heated remnant of a core-collapse supernova, it is fundamentally a radiation hydrodynamics problem (although the regions important for neutrino emission are not very *dynamic* after bounce). Over time, the treatment of radiative transfer and neutrino microphysics in simulations has become increasingly sophisticated, moving from the equilibrium flux limited diffusion (EFLD) and greatly simplified neutrino physics (Burrows & Lattimer 1986) to full solutions of the Boltzmann equation (Fischer et al. 2010) with more realistic microphysics (H  depohl et al. 2010).

Here, a new fully implicit code is developed for calculating the detailed evolution of PNSs in spherically symmetric general relativity within a variable Eddington factor formalism. The structure of the paper is as follows: In section 2, the equations of neutrino transport within the projected symmetric trace-free moment formalism of Thorne (1981) are described, and generic neutrino source terms for this formalism are derived. In section 3, a method for obtaining closure relations for the moment equations via a formal solution of the Boltzmann equation are described. A fully implicit numerical implementation of neutrino transport coupled to hydrodynamics/hydrostatics is described in section 4 (with code tests described in appendix A). A fiducial model of PNS cooling is detailed in section 5. These results are compared with the results of an EFLD calculation of PNS cooling in section 6.1. The implications of these new calculations of PNS cooling on the composition of the neutrino driven wind are discussed in section 6.2. In section 6.3, the properties of the integrated neutrino emission are discussed. The convention $\hbar = c = G = 1$ is adopted in sections 2 through 4 to avoid a plethora of factors. In section 6.2, units with $\hbar = c = 1$ are used.

2. THE MOMENT APPROACH TO GENERAL RELATIVISTIC RADIATIVE TRANSFER

The equations of radiative transfer in curved spacetimes were first derived by Lindquist (1966), which described the evolution of the invariant distribution function along geodesics in phase space. The general form of the general relativistic Boltzmann (or Lindquist) equation in the absence of external forces is

$$\frac{df(x^\mu, p^\nu(x^\mu))}{d\tau} = p^\beta \left(\frac{\partial f}{\partial x^\beta} - \Gamma_{\beta\gamma}^\alpha p^\gamma \frac{\partial f}{\partial p^\alpha} \right) = \left(\frac{df}{d\tau} \right)_{\text{coll}}, \quad (1)$$

where f is the invariant distribution function, p^β is the neutrino four-momentum (which is constrained to be on mass shell), and $\Gamma_{\beta\gamma}^\alpha$ are the Christoffel symbols. The collision term on the right hand side describes the destruction and production of neutrinos on a particular phase-space trajectory by capture processes, pair annihilation, scattering, and their inverses. In addition to describing the propagation of neutrinos along trajectories in physical space, this also encodes the evolution of the energy of neutrinos along geodesics of the spacetime. In three spatial dimensions, this is a seven dimensional equation that needs to be solved for each neutrino species.

A number of numerical strategies can be employed to solve the transport problem (Mihalas & Mihalas 1984). Foremost among these are discrete ordinate methods, where the Boltzmann equation is directly discretized in momentum space as well as in physical space (e.g. Yueh & Buchler 1977; Mezzacappa & Messer 1999; Liebend  rfer et al. 2004), and moment-based approaches, where angular integrations of the Boltzmann equation in momentum space are performed (e.g. Thorne 1981; Burrows et al. 2000; Rampp & Janka 2002). These two approaches give similar results in one-dimensional models, at least in the context of core-collapse supernovae (Liebend  rfer et al. 2005). An additional technique that has only been employed for solving static problems in the supernova context, but is perhaps the most capable of retaining fidelity to the underlying Boltzmann equation, is Monte Carlo neutrino transport (Janka & Hillebrandt 1989; Keil et al. 2003).

The moment approach results in an infinite hierarchy of coupled equations which needs to be truncated at some order in practice. Generally, only the zeroth and first order moment equations are retained and a closure relation is assumed between the first two moments and the higher order moments that enter the first two moment equations. Such schemes are referred to as variable Eddington factor methods (Mihalas & Mihalas 1984). When only the first two moments are used, the number of equations relative to discrete ordinate methods is significantly reduced, easing the computational burden (especially in an implicit scheme like the one described below). Of course, this gain in computational efficiency is useful only if reasonable closures can be obtained. The closure relations only encode information about the angular distribution of neutrinos, so that the approximations involved in solving a linearized Boltzmann equation do not severely impact the fidelity of numerical calculations to the true solution (Mihalas & Mihalas 1984; Ensman 1994).

Here a variable Eddington factor approach to radiative transfer is employed, with the closure relations being obtained from a formal solution of the static relativistic Boltzmann equation. This approach is similar to that used by Burrows et al. (2000) and Rampp & Janka (2002), except for being fully general relativistic, incorporating both inelastic scattering and pair production (in contrast to only the former), using energy integrated groups rather than energy ‘‘pickets’’, and in the specific method of finding the closure relations. The formalism for this method is described below.

The moments of the Boltzmann equation also most naturally give the various forms of the diffusion approximation, which has been used in the majority of PNS studies (Burrows & Lattimer 1986; Keil & Janka 1995;

Pons *et al.* 1999; Roberts *et al.* 2012) and in a significant fraction of studies of the early core-collapse and bounce phases (Bruenn 1985; Wilson & Mayle 1993). The formalism is connected to EFLD in appendix B.

2.1. General Relativistic Generalities

In spherical symmetry, it is simplest to work in a coordinate system that anticipates a Lagrangian frame for the fluid. The metric for such a space-time is given by (Misner & Sharp 1964)

$$ds^2 = -e^{2\phi} dt^2 + \left(\frac{r'}{\Gamma}\right)^2 da^2 + r^2 d\Omega^2, \quad (2)$$

where ds is the invariant interval, t is the time measured at infinity, r is the areal radius, Ω is the solid angle, and Γ and ϕ are metric potentials. Coordinate freedom can be exploited to choose this frame to be the rest-frame of the fluid, which demands (Liebendörfer *et al.* 2001a)

$$\frac{\partial r}{\partial a} = \frac{\Gamma}{4\pi r^2 n_B}. \quad (3)$$

Here, n_B is the baryon number density and

$$\Gamma = \sqrt{1 + u^2 - \frac{2m}{r}} \quad (4)$$

where u and m are defined below. With this choice, the orthonormal frame associated with the coordinate frame is just the rest frame of the fluid and da is just the change in enclosed baryon number with the physical volume. Therefore, this formulation is working in the Lagrangian frame, as claimed.

The equations of spherically symmetric general relativistic hydrodynamics and the Einstein equation are recorded for convenience (Misner & Sharp 1964). Most of these results are nicely presented and detailed in similar form by Liebendörfer *et al.* (2001a). The time evolution of the areal radius is given by,

$$\frac{\partial r}{\partial t} = e^{\phi} u \quad (5)$$

which defines u . The evolution of u is given by

$$\frac{\partial u}{\partial t} = \Gamma^2 \frac{\partial e^{\phi}}{\partial r} - e^{\phi} \frac{m + 4\pi r^3(p + Q)}{r^2}, \quad (6)$$

where Q is the viscosity and p is the pressure of the fluid. This gives the equation of hydrostatic balance when the left hand side equals zero (i.e. the Tolman-Oppenheimer-Volkov equation (Oppenheimer & Volkoff 1939)). The enclosed gravitational mass, m , is defined by

$$\frac{\partial m}{\partial a} = \Gamma \left(\frac{E}{n_B} + \epsilon \right) + u \frac{H}{n_B}, \quad (7)$$

where ϵ is the internal energy per baryon, E is the total neutrino energy density in the rest frame, and H is the net radial energy flux from neutrinos. The constraint equation for the metric potential ϕ is

$$\frac{\epsilon}{e^{\phi}} \frac{\partial e^{\phi}}{\partial a} + \frac{1}{n_B e^{\phi}} \frac{\partial (e^{\phi} p)}{\partial a} + \frac{1}{r^3 n_B e^{\phi}} \frac{\partial (r^3 e^{\phi} Q)}{\partial a} = 0, \quad (8)$$

where a small time dependent term has been neglected.

The transport equations described in the next section are formulated in a congruence corresponding to the four-velocity field of the PNS (clearly, this is not a geodesic congruence). The behavior of this congruence is best

described by expanding the covariant derivative of the four-velocity as

$$U_{\mu;\nu} = -a_{\nu} U_{\mu} + \frac{\Theta}{3} P_{\mu\nu} + \sigma_{\mu\nu} + \omega_{\mu\nu}, \quad (9)$$

where U_{μ} is the tangent four-vector field of the congruence, $P_{\mu\nu}$ is the projection tensor (which projects into the vector subspace orthogonal to U^{μ}) $a^{\nu} = U^{\alpha} U_{;\alpha}^{\nu}$ is the acceleration, $\Theta = U^{\mu}_{;\mu}$ is the expansion, $\sigma_{\mu\nu}$ is the shear, and $\omega_{\mu\nu}$ is the rotation. Using the continuity equation, the expansion of the congruence becomes

$$\Theta = -D_{\hat{t}} \ln(n_B). \quad (10)$$

In spherical symmetry, the acceleration four-vector is parallel to the radial orthonormal basis vector, so that only the scalar acceleration is needed

$$a = \Gamma \frac{\partial \phi}{\partial r}. \quad (11)$$

In spherical symmetry, the shear is characterized by a single component, the scalar shear

$$\sigma = -\frac{2u}{r} - \frac{2}{3}\Theta. \quad (12)$$

Additionally, such a spherically symmetric congruence possesses no rotation, so that $\omega_{\mu\nu} = 0$. The quantity

$$b = \frac{\Gamma}{r} \quad (13)$$

will also be required, which is related to the extrinsic curvature (Thorne 1981). The orthonormal frame temporal and radial derivative operators are

$$D_{\hat{t}} = e^{-\phi} \frac{\partial}{\partial t} \quad (14)$$

and

$$D_{\hat{r}} = 4\pi r^2 n_B \frac{\partial}{\partial a} = \Gamma \frac{\partial}{\partial r}. \quad (15)$$

2.2. Variable Eddington Factor Transport Equations

Here, the evolution equations for the neutrino number density, energy density, number flux and energy flux are derived from the zeroth and first order moments of the relativistic Boltzmann equation. The basic results are taken from the spherically symmetric version of the projected symmetric trace-free moment formalism of Thorne (1981). This formalism reduces to an expansion of the neutrino distribution function in terms of Legendre polynomials in a flat space-time.

The moments of the distribution function are defined in spherical symmetry as

$$w^n = \frac{\omega^3}{(2\pi)^2} B_n \int_{-1}^1 d\mu P_n(\mu) f(\omega, \mu) \quad (16)$$

where

$$B_n = \frac{n!(2n+1)}{(2n+1)!!}, \quad (17)$$

P_n are the Legendre polynomials, and ω is the neutrino energy in the fluids rest frame. The first two moment equations in spherical symmetry can be read off from equation 5.10 of Thorne (1981)

$$w_{,\hat{t}}^0 + \frac{4}{3}\Theta w^0 + \frac{3}{2}\sigma w^2 + w_{,\hat{r}}^1 \\ 2(a+b)w^1 - \frac{\partial}{\partial \omega} \omega \left[a w^1 + \frac{\Theta}{3} w^0 + \frac{3}{2} \sigma w^2 \right] = s^0 \quad (18)$$

and

$$w_{,\hat{r}}^2 + (a + 3b)w^2 + w_{,\hat{t}}^1 + \left[\frac{4}{3}\Theta + \sigma\right]w^1 + \frac{1}{3}w_{,\hat{r}}^0 + \frac{4}{3}aw^0 - \frac{\partial}{\partial\omega} \left[aw^2 + \left(\frac{\Theta}{3} + \frac{2}{5}\sigma\right)w^1 + \frac{1}{3}aw^0 + \frac{3}{2}\sigma w^3\right] = s^1 \quad (19)$$

where s^l are the neutrino source terms defined in section 2.3. To close this system, define the Eddington like factors

$$g_2 = w^2/w^0 \quad (20)$$

$$g_3 = w^3/w^1 \quad (21)$$

which both go to zero in the limit $f(\mu) = f_0 + \mu f_1$, which corresponds to the diffusion regime. Note that these differ from the standard definition of the Eddington factors (Rampp & Janka 2002), which is due to how I have chosen to calculate the moments. For free streaming radiation in a flat background $g_2 = 2/3$, and these equations reduce to the linear wave equation for $h = h(r \pm t) \equiv r^2 w_0$. A method for approximating these Eddington factors is detailed in section 3.

For problems that are close to being static on the radiation timescale, it is useful to switch the independent variable ω , the energy in the fluid rest frame, of w^i to the energy at infinity, ν (c.f. Schinder & Bludman 1989). In the case of PNS cooling, the energy at infinity is much closer to being a constant of the motion and therefore a more natural variable. Additionally, this choice simplifies the formal solution of the Boltzmann equation. The moments of the distribution function are then

$$w^i = w^i(r, \nu(\omega, r, t)) \quad (22)$$

where the energy at infinity is defined as $\nu = e^{\phi(r,t)}\omega$. This means that the replacement

$$\frac{\partial w^i}{\partial x} \rightarrow \frac{\partial w^i}{\partial x} + \frac{\partial \nu}{\partial x} \frac{\partial w^i}{\partial \nu} \quad (23)$$

needs to be made for all radial and time derivatives, resulting in

$$\begin{aligned} & \frac{\partial w^0/n_B}{\partial t} + \frac{w^0}{n_B} e^{\phi} \left(\frac{\Theta}{3} + g_2 \frac{3}{2} \sigma \right) + \frac{\partial}{\partial a} (4\pi r^2 e^{\phi} w^1) \\ & - \frac{e^{\phi}}{n_B} \frac{\partial}{\partial \nu} \nu \left[\left(\frac{\Theta}{3} + g_2 \frac{3}{2} \sigma \right) w^0 \right] + \frac{\nu}{n} \frac{\partial \phi}{\partial t} \frac{\partial w^0}{\partial \nu} = e^{\phi} \frac{s^0}{n_B} \end{aligned} \quad (24)$$

and

$$\begin{aligned} & e^{-\phi} \frac{\partial w^1}{\partial t} + \left[\frac{4}{3} \Theta + \sigma \right] w^1 + n_B e^{-\phi} \frac{\partial}{\partial a} \left[4\pi r^2 e^{\phi} \left(\frac{1}{3} + g_2 \right) w^0 \right] \\ & + \left(\frac{2}{3} - g_2 \right) (a - b) w^0 - \frac{\partial}{\partial \nu} \nu \left[\left(\frac{\Theta}{3} + \frac{2}{5} \sigma + \frac{3}{2} \sigma g_3 \right) w^1 \right] \\ & + e^{-\phi} \frac{\partial \phi}{\partial t} \nu \frac{\partial w^1}{\partial \nu} = s^1. \end{aligned} \quad (25)$$

To easily deal with optically thick regions where the distribution function may possess a sharp Fermi surface, energy integrated groups are used rather than discrete energy “pickets”. The group numbers, energies, number fluxes, energy fluxes, and source terms in group g are defined by

$$N_g = \int_{\omega_{g,L}}^{\omega_{g,U}} \frac{d\omega}{\omega} w^0, F_g = \int_{\omega_{g,L}}^{\omega_{g,U}} \frac{d\omega}{\omega} w^1,$$

$$\begin{aligned} S_g^0 &= \int_{\omega_{g,L}}^{\omega_{g,U}} \frac{d\omega}{\omega} s^0, S_g^1 = \int_{\omega_{g,L}}^{\omega_{g,U}} \frac{d\omega}{\omega} s^1, \\ E_g &= \int_{\omega_{g,L}}^{\omega_{g,U}} d\omega w^0, H_g = \int_{\omega_{g,L}}^{\omega_{g,U}} d\omega w^1, \\ Q_g^0 &= \int_{\omega_{g,L}}^{\omega_{g,U}} d\omega s^0, \text{ and } Q_g^1 = \int_{\omega_{g,L}}^{\omega_{g,U}} d\omega s^1. \end{aligned} \quad (26)$$

Here, $\omega_{g,L}$ is the lower energy bound of an energy group and $\omega_{g,U}$ is the upper bound. Integrating over energy at infinity within groups gives

$$N_g = \int_{\nu_{L,g}}^{\nu_{U,g}} \frac{d\nu}{\nu} w^0 \text{ and } E_g = e^{-\phi} \int_{\nu_{L,g}}^{\nu_{U,g}} d\nu w^0 \quad (27)$$

and similar expressions for F_g , H_g , and the source terms. The operators $\int d\nu/\nu$ and $\int d\nu$ can then be applied to the “red shifted” equations. The evolution the neutrino group number densities are described by

$$\begin{aligned} & \frac{\partial}{\partial t} \left(\frac{N_g}{n_B} \right) + \frac{\partial}{\partial a} (4\pi r^2 e^{\phi} F_g) \\ & - \frac{e^{\phi}}{n_B} \left(\frac{\Theta}{3} + g_2 \frac{3}{2} \sigma - e^{-\phi} \frac{\partial \phi}{\partial t} \right) w^0 \Big|_{\nu_L}^{\nu_U} = e^{\phi} \frac{S_g^0}{n_B}. \end{aligned} \quad (28)$$

The last term on the left hand side describes the red or blue shifting of neutrinos to other groups via compression and time variation of the metric potential ϕ . If the group comprises energies from zero to infinity, the red shifting terms drop out and one is left with the standard number transport equation given in Pons *et al.* (1999). Applying the number operator to equation 25 and simplifying gives

$$\begin{aligned} & e^{-\phi} \frac{\partial F_g}{\partial t} + \left[\Theta + \left(\frac{3}{5} - \frac{3}{2} g_2 \right) \sigma \right] F_g \\ & + \frac{r^2 n_B}{3e^{3\phi}} \frac{\partial}{\partial a} (4\pi e^{3\phi} N_g) + \frac{n_B}{r} \frac{\partial}{\partial a} (4\pi r^3 g_2 E_g) \\ & - \left[\frac{\Theta}{3} + \left(\frac{2}{5} + \frac{3}{2} g_2 \right) \sigma - e^{-\phi} \frac{\partial \phi}{\partial t} \right] w^1 \Big|_{\nu_L}^{\nu_U} = S_g^1. \end{aligned} \quad (29)$$

This includes similar terms to equation 28, plus a term that includes the effects of compression on the total number flux. The energy group evolution equations are

$$\begin{aligned} & \frac{\partial}{\partial t} \left(\frac{E_g}{n_B} \right) + e^{\phi} \left(\frac{\Theta}{3} + g_2 \frac{3}{2} \sigma \right) \frac{E_g}{n_B} + e^{-\phi} \frac{\partial}{\partial a} (4\pi r^2 e^{2\phi} H_g) \\ & - \frac{1}{n_B} \left(\frac{\Theta}{3} + g_2 \frac{3}{2} \sigma - e^{-\phi} \frac{\partial \phi}{\partial t} \right) (\nu w^0) \Big|_{\nu_L}^{\nu_U} = e^{\phi} \frac{Q_g^0}{n_B}. \end{aligned} \quad (30)$$

Aside from the addition of a compression term and different factors of e^{ϕ} , this is identical to equation 28. The energy flux group evolution equations are

$$\begin{aligned} & e^{-\phi} \frac{\partial H_g}{\partial t} + \left[\frac{4}{3} \Theta + \sigma \right] H_g \\ & + \frac{r^2 n_B}{3e^{4\phi}} \frac{\partial}{\partial a} (4\pi e^{4\phi} E_g) + \frac{n_B}{re^{\phi}} \frac{\partial}{\partial a} (4\pi r^3 e^{\phi} g_2 E_g) \\ & - \left(\frac{\Theta}{3} + \frac{2}{5} \sigma + g_3 \frac{3}{2} \sigma - e^{-\phi} \frac{\partial \phi}{\partial t} \right) (\nu w^1) \Big|_{\nu_L}^{\nu_U} = Q_g^1 \end{aligned} \quad (31)$$

The numerical implementation of the red-shifting terms is described in section 4.6.

Additionally, neutrinos have a back-reaction on the matter they are propagating through by exchanging energy, lepton number, and momentum with the background medium. Assuming that the background possesses a thermal state, the first law of thermodynamics for the medium can be combined with the sum of equations 30 over all groups to find an equation for the conservation of total internal energy

$$\begin{aligned} & \frac{\partial}{\partial t} \left(\epsilon + \sum_{g,s} \frac{E_{g,s}}{n} \right) + e^\phi \Theta \left(\frac{p}{n} + \sum_{g,s} \frac{E_{g,s}}{3n} \right) \\ & + \frac{3e^\phi}{2} \sigma \sum_{g,s} g_{2,g} \frac{E_{g,s}}{n} + e^{-\phi} \frac{\partial}{\partial a} \left(4\pi r^2 e^{2\phi} \sum_{g,s} H_{g,s} \right) \end{aligned} \quad (32)$$

where the sums are over groups and species. Obviously, the neutrino energy source terms have exactly canceled with the source terms for the medium.

In the absence of neutrinos, the electron fraction of the background medium is fixed, i.e. $e^{-\phi} \dot{Y}_e = 0$. When neutrinos are included, interactions of electron flavored neutrinos exchange lepton number with the background, yielding $e^{-\phi} \dot{Y}_e = -\sum_g S_g^0/n_B$. The total lepton number of the medium is given by $Y_L = Y_e + \sum_g [N_{g,\nu_e} - N_{g,\bar{\nu}_e}]/n_B$. Combining the evolution equation for Y_e with equations 28 gives the lepton number evolution equation

$$\begin{aligned} & \frac{\partial}{\partial t} \left(Y_e + \sum_g \left[\frac{N_{g,\nu_e}}{n_B} - \frac{N_{g,\bar{\nu}_e}}{n_B} \right] \right) \\ & + \frac{\partial}{\partial a} \left(4\pi r^2 e^\phi \sum_g [F_{g,\nu_e} - F_{g,\bar{\nu}_e}] \right) = 0. \end{aligned} \quad (33)$$

This constitutes the full set of evolution equations for the state of the medium including non-thermal neutrinos of all flavors, when the Eddington factors g_2 and g_3 are specified.

2.3. Neutrino Source Terms

The collision term in equation 1 describes how neutrinos move from one trajectory to another via scattering and how they are created and destroyed by the underlying medium. For the PNS problem these processes include neutral current scattering off of electrons, nucleons, and nuclei (Reddy et al. 1998), neutrino pair production via nucleon-nucleon bremsstrahlung (Hannestad & Raffelt 1998) and electron-positron annihilation (Bruenn 1985), and charged current processes involving electron and anti-electron flavor neutrinos and neutrons and protons, respectively (Reddy et al. 1998).

The details of these microphysical processes are eschewed by assuming that the differential cross-sections for these processes are known and referring the reader to the papers cited above, as well as the review Burrows et al. (2006). The exact details of the microphysics used in the code will be reported in a future publication, although certain aspects are discussed in sections 5 and 6.2. Many of the results in this section are well known (e.g. Bruenn 1985; Pons et al. 1999), and are included here for completeness and to make clear

the details of the exact implementation within the integrated energy group formalism described above. Explicit detailed balancing (independent of the choice of underlying scattering kernels) is emphasized.

The source function for a particular moment is given by

$$\begin{aligned} s^l &= \frac{\omega^3}{(2\pi)^2} B_l \int_{-1}^1 d\mu P_l(\mu) \\ &\times \left(j_a(1-f) - \frac{f}{\lambda_a} + j_s(1-f) - \frac{f}{\lambda_s} + j_p(1-f) - \frac{f}{\lambda_p} \right) \end{aligned} \quad (34)$$

which includes contributions from absorption ($1/\lambda_a$), scattering ($1/\lambda_s$), pair-annihilation ($1/\lambda_p$), and their inverses (j_a, j_s , and j_p). The choice of metric and reference frame implies that the scattering kernels should be evaluated in the rest frame of the fluid, simplifying things compared to hybrid frame approaches (Hubeny & Burrows 2007).

For the absorption part, using the standard detailed balance relations gives

$$j_a(1-f) - \frac{f}{\lambda_a} = \frac{1}{\lambda_a^*} (f_{eq}(\omega, T, \mu_{eq}) - f(\omega, \mu)), \quad (35)$$

where $\lambda_a^{*-1} = [1 + \exp\{-(\omega - \mu_{eq})/T\}]\lambda_a^{-1}$ and f_{eq} is a Fermi-Dirac distribution. The scattering contributions are

$$j_s = \int \frac{d\omega'}{(2\pi)^3} \omega'^2 \int_{-1}^1 d\mu' \int_0^{2\pi} d\phi' R^s(\omega', \omega, \mu') f(\omega', \mu_{out}) \quad (36)$$

and

$$\lambda_s = \int \frac{d\omega'}{(2\pi)^3} \omega'^2 \int_{-1}^1 d\mu' \int_0^{2\pi} d\phi' R^s(\omega, \omega', \mu') (1 - f(\omega', \mu_{out})), \quad (37)$$

and the pair-annihilation contributions are

$$j_p = \int \frac{d\omega'}{(2\pi)^3} \omega'^2 \int_{-1}^1 d\mu' \int_0^{2\pi} d\phi' R_{in}^p(\omega, \omega', \mu') (1 - \bar{f}(\omega', \mu_{out})) \quad (38)$$

and

$$\lambda_p = \int \frac{d\omega'}{(2\pi)^3} \omega'^2 \int_{-1}^1 d\mu' \int_0^{2\pi} d\phi' R_{out}^p(\omega, \omega', \mu') \bar{f}(\omega', \mu_{out}). \quad (39)$$

The outgoing cosine is given by $\mu_{out} = \mu\mu' - \sqrt{1-\mu^2}\sqrt{1-\mu'^2}\cos\phi'$. The R_{out} functions are related to the differential cross-section by

$$R(\omega, \omega', \mu) = \frac{(2\pi)^2}{\omega'^2} \frac{1}{V} \frac{d\sigma}{d\omega' d\mu}, \quad (40)$$

with no phase space blocking term for the final neutrinos in the differential cross-section. The R functions obey the detailed balance relations for scattering

$$R^s(\omega, \omega', \mu) = R^s(\omega', \omega, \mu) e^{(\omega - \omega')/T}. \quad (41)$$

and annihilation

$$R_{out}^p(\omega, \omega', \mu) = R_{in}^p(\omega, \omega', \mu) e^{(\omega + \omega')/T} \equiv R^p(\omega, \omega', \mu). \quad (42)$$

For use in the moment formalism, R must be expanded in terms of the Legendre polynomials as

$$R(\omega, \omega', \mu') = \sum_{l=0}^{\infty} R_l(\omega, \omega') P_l(\mu'). \quad (43)$$

The distribution function, f , is also expanded in a similar way. In general, this results in integrals of the form

$$\begin{aligned} F_{klmn} &= \int_{-1}^1 d\mu \int_{-1}^1 d\mu' \int_0^{2\pi} d\phi' P_k(\mu') P_l(\mu) P_m(\mu) \\ &\quad \times P_n(\mu\mu' - \sqrt{1-\mu^2}\sqrt{1-\mu'^2}\cos\phi') \\ &= 2\pi \frac{\delta_{kn}}{2n+1} I_{lmn}. \end{aligned} \quad (44)$$

where $I_{lmn} = \int_{-1}^1 d\mu P_l(\mu) P_m(\mu) P_n(\mu)$. For a more detailed description of such an expansion, see Mezzacappa & Bruenn (1993).

Using this expansion, the scattering contribution to the source term is given by

$$\begin{aligned} s_s^l &= \frac{4\omega^3}{(2\pi)^4} B_l \int d\omega' \omega'^2 \\ &\quad \times \left\{ \frac{R_l^s f_l'}{(2l+1)^2} e^{-(\omega-\omega')/T} - \frac{R_0^s f_l}{2l+1} \right. \\ &\quad \left. + \frac{1}{2} \sum_{m,n=0}^{\infty} R_n^s f_m' f_n \frac{I_{lmn}}{2n+1} \left(1 - e^{-(\omega-\omega')/T}\right) \right\} \end{aligned} \quad (45)$$

and the pair annihilation contribution is given by

$$\begin{aligned} s_p^l &= \frac{4\omega^3}{(2\pi)^4} B_l \int d\omega' \omega'^2 e^{-(\omega+\omega')/T} \\ &\quad \times \left\{ R_0^p \delta_{0l} - \frac{R_0^p f_l}{2l+1} - \frac{R_l^p \bar{f}_l'}{(2l+1)^2} \right. \\ &\quad \left. + \frac{1}{2} \sum_{m,n=0}^{\infty} R_n^p f_m \bar{f}_n' \frac{I_{lmn}}{2n+1} \left(1 - e^{-(\omega+\omega')/T}\right) \right\} \end{aligned} \quad (46)$$

Clearly, all of the moments are coupled to all of the other moments by the source terms in addition to the coupling present on the LHS of the moment equations. Practically, this series must be truncated at some finite order. It is standard to use only the zeroth and first moment (Burrows et al. 2006). This convention is followed, but with the caveat that this may not be a good approximation for the annihilation terms near the free streaming regime (Pons et al. 1998).

2.3.1. Zeroth Order Source Function

Now the three contributions to the source functions for the number and energy group equations are considered separately. Special attention is given to assuring that the chosen forms for the source terms *explicitly* push the neutrinos towards equilibrium, independent of the chosen opacity functions.

The absorption part of the source function is given by

$$S_{a,g}^0 = \left\langle \frac{1}{\lambda_a^*} \right\rangle_g [G_g - N_g], \quad (47)$$

and

$$Q_{a,g}^0 = \left\langle \frac{1}{\lambda_a^*} \right\rangle_g [B_g - E_g], \quad (48)$$

where

$$B_g = \int_{\omega_L^g}^{\omega_U^g} d\omega \frac{2\omega^3}{(2\pi)^2} \frac{1}{e^{(\omega-\mu_{\text{eq}})/T} + 1}, \quad (49)$$

and

$$G_g = \int_{\omega_L^g}^{\omega_U^g} d\omega \frac{2\omega^2}{(2\pi)^2} \frac{1}{e^{(\omega-\mu_{\text{eq}})/T} + 1}. \quad (50)$$

The average over the inverse absorption mean free path can be performed in a number of ways. For small enough energy intervals for groups, the mean free path for the central energy of the group can be taken. It can also be assumed that the energy within a group is distributed as in a blackbody, but renormalized to the total energy within the group. Then the averaged inverse mean free path is analogous to the Planck mean opacity, but using a Fermi-Dirac distribution instead of a Planck distribution. Independent of the averaging procedure chosen, this term serves to push the neutrino energy density towards equilibrium with the background medium.

To find the scattering contribution to the zero order moment equation, it is assumed that the distribution of energy within a particular energy group is proportional to the blackbody distribution. Using this ansatz in equation 45 and then averaging over group energies gives scattering term

$$\begin{aligned} S_{s,g}^0 &= \sum_{g'} \Phi_{0,gg'}^s N_{g'} \left(\frac{D_{g'}}{G_{g'}} - 1 \right) (D_g - N_g) \\ &\quad - \Phi_{0,gg'}^s N_g \left(\frac{D_g}{G_g} - 1 \right) (D_{g'} - N_{g'}) \\ &\quad + \Phi_{1,gg'}^s F_g F_{g'} \left(\frac{D_g}{G_g} - \frac{D_{g'}}{G_{g'}} \right), \end{aligned} \quad (51)$$

and

$$\begin{aligned} Q_{s,g}^0 &= \sum_{g'} \Phi_{0,gg'}^s N_{g'} \left(\frac{D_{g'}}{G_{g'}} - 1 \right) (C_g - E_g) \\ &\quad - \Phi_{0,gg'}^s E_g \left(\frac{C_g}{B_g} - 1 \right) (D_{g'} - N_{g'}) \\ &\quad + \Phi_{1,gg'}^s H_g F_{g'} \left(\frac{C_g}{B_g} - \frac{D_{g'}}{G_{g'}} \right), \end{aligned} \quad (52)$$

where

$$C_g = \int_{\omega_L^g}^{\omega_U^g} d\omega \frac{2\omega^3}{(2\pi)^2}, \text{ and } D_g = \int_{\omega_L^g}^{\omega_U^g} d\omega \frac{2\omega^2}{(2\pi)^2}. \quad (53)$$

The averaged scattering kernel is defined as

$$\Phi_{l,gg'}^s = \left\langle R_l(\omega, \omega') e^{-(\omega-\mu_{\nu, \text{eq}})/T} \right\rangle_{\Delta E_g, \Delta E_{g'}}, \quad (54)$$

where the average is taken over the energies of the incoming and outgoing groups. This has the useful property $\Phi_{l,gg'}^s = \Phi_{l,g'g}^s$, which derives from the detailed balance criterion given above. This form of the scattering source term naturally conserves neutrino number, although it does not push the neutrino numbers toward the expected distribution for a purely scattering process. Both source terms go to zero when neutrinos are in both chemical and energy equilibrium with the medium. The energy exchange expression does not go to zero when $g' = g$. Although it might be naively assumed that this corresponds to elastic scattering and therefore not contribute to the evolution of the group energy, there are in fact contributions from small energy transfer scatterings to

this term as well. Although these will conserve neutrino number within the group, they can result in energy exchange with the medium. This allows the formalism to somewhat naturally deal with energy transfer due to scattering off nucleons, which generally exchanges energy on a scale that is smaller than the group spacing. The weighting function for the average over the groups necessarily involves some level of approximation. The natural incorporation of equilibrium far outweighs the small error introduced due to the approximate weighting of the scattering kernel.

Using a similar procedure to the one used for the scattering source term, the energy integrated pair production/annihilation source term is given by

$$S_{p,g}^0 = \sum_{g'} \Phi_{0,gg'}^p (D_{g'}^0 - \bar{N}_{g'}) (D_g^0 - N_g) - \Phi_{0,gg'}^p N_g \bar{N}_{g'} (D_{g'}^0 / \bar{G}_{g'} - 1) (D_g^0 / G_g - 1) + \Phi_{1,gg'}^p F_g \bar{F}_{g'} (1 - e^{(\omega+\omega')/T}), \quad (55)$$

where the over bar denotes the energy density and flux of a neutrinos anti-species. This term once again naturally goes to zero when thermal equilibrium is reached (i.e. when $N_g = G_g$ and $F_g = 0$). Here,

$$\Phi_{i,gg'}^p = \left\langle e^{-(\omega+\omega')/T} R_i^p(\omega, \omega') \right\rangle_{\Delta E_g, \Delta E_{g'}}. \quad (56)$$

The source term Q_p^1 can be obtained from the above equation by the replacements $F_g \rightarrow H_g$, $N_g \rightarrow E_g$, $D_g \rightarrow C_g$, and $G_g \rightarrow B_g$, while leaving the g' terms unchanged.

2.3.2. First Order Source Function

For the first order source function terms, one does not need to be as careful about getting forms that explicitly go to zero in equilibrium as all terms end up being proportional to the first order distribution function and therefore satisfy this constraint automatically.

The absorption contribution to the first order source function is

$$S_a^1 = -F_g \left\langle \frac{1}{\lambda_a^*} \right\rangle_g, \quad (57)$$

and

$$Q_a^1 = -H_g \left\langle \frac{1}{\lambda_a^*} \right\rangle_g. \quad (58)$$

The scattering source term in equation 28 is

$$S_s^1 = \sum_{g'} \Phi_{0,gg'}^s F_g \left[N_{g'} \left(\frac{D_g}{G_g} - \frac{D_{g'}}{G_{g'}} \right) - D_{g'} \left(\frac{D_g}{G_g} - 1 \right) \right] + \frac{\Phi_{1,gg'}^s F_{g'}}{3} \left[N_g \left(\frac{D_g}{G_g} - \frac{D_{g'}}{G_{g'}} \right) + D_g \left(\frac{D_{g'}}{G_{g'}} - 1 \right) \right] \quad (59)$$

The source term Q_s^1 can be obtained from the above equation by the replacements $F_g \rightarrow H_g$, $N_g \rightarrow E_g$, $D_g \rightarrow C_g$, and $G_g \rightarrow B_g$, while leaving the g' terms unchanged. When scattering is iso-energetic, this reduces to

$$S_{s,\text{iso-en}}^1 = -F_g \frac{2\omega^2}{(2\pi)^2} \left[\tilde{R}_0^s(\omega) - \tilde{R}_1^s(\omega)/3 \right] \equiv -H_g [\chi_0^s(\omega) - \chi_1^s(\omega)/3] \quad (60)$$

where \tilde{R}_i^s is the iso-energetic scattering kernel.

The first order moment equation pair annihilation source term is

$$S_p^1 = \sum_{g'} \Phi_{0,gg'}^p F_g \left[\bar{N}_{g'} (1 - e^{\beta(\omega+\omega')}) - D_{g'}^0 \right] + \frac{\Phi_{1,gg'}^s \bar{F}_{g'}}{3} \left[N_g (1 - e^{\beta(\omega+\omega')}) - D_g^0 \right], \quad (61)$$

and Q_p^1 can be found the same replacement required to find S_s^1 from Q_s^1 .

3. FORMAL SOLUTION OF THE BOLTZMANN EQUATION

To get the factors g_2 and g_3 , an angle dependent version of the Boltzmann equation needs to be solved. First, note that the outer layers of the PNS are in tight radiative equilibrium throughout the duration of the simulation. Therefore, all time dependence can be reasonably dropped in the equation of radiative transfer if one is only interested in the ratios of various moments. Of course, such an approximation breaks down in highly dynamical situations. For such circumstances, a closure scheme like the one described in Rampp & Janka (2002) is more appropriate. This time-independent formulation of the formal solution, which makes calculation of the Eddington factors significantly easier, is similar to the approach advocated by Ensman (1994), except that it incorporates general relativistic affects, such as the bending of geodesics. Schinder & Bludman (1989) describe a similar, but time-dependent formulation.

In a spherically symmetric static spacetime, the equation of radiative transfer is (Lindquist 1966)

$$\Gamma \left[\mu \frac{\partial}{\partial r} + (1 - \mu^2) \left\{ \frac{1}{r} - \frac{\partial \phi}{\partial r} \right\} \frac{\partial}{\partial \mu} \right] f(\nu, \mu, r) = \frac{1}{\lambda_a^*} [f_{eq}(r) - f(\nu, \mu, r)] + j_s[f](1 - f(\nu, \mu, r)) - \lambda_s^{-1}[f]f(\nu, \mu, r). \quad (62)$$

Here, the neutrino distribution function, f , has been written in terms of the energy of the neutrinos at infinity, ν , and μ is the cosine of the angle of neutrino propagation relative to the radial vector.

A formal solution to equation 62 can easily be found using the method of characteristics. The characteristic equations are

$$d\lambda \equiv \frac{dr}{\Gamma\mu} = \frac{d\mu}{\Gamma(1 - \mu^2)(1/r - \frac{\partial \phi}{\partial r})} = df / \left(\frac{df}{d\lambda} \right)_{coll} \quad (63)$$

where λ is the physical path length. The second equality is easily integrated to find a relationship between r and μ along a geodesic. Any geodesic can be characterized by the radius at which $\mu = 0$. First, define the quantity

$$\beta = r_m e^{-\phi_m}, \quad (64)$$

where the subscript m denotes the minimum radius of propagation. This is just the impact parameter of the trajectory. Then, for a given β and r , the angle of propagation along a geodesic is given by

$$\mu = \pm \sqrt{1 - \left(\frac{\beta e^\phi}{r} \right)^2}. \quad (65)$$

The first equality in the characteristic equations can be integrated to find the physical path length between any two radii for a particular characteristic if Γ and ϕ are assumed constant over this distance, giving

$$\Delta\lambda \approx \pm\Gamma^{-1} \left[\sqrt{r_f^2 - e^{2\phi}\beta^2} - \sqrt{r_i^2 - e^{2\phi}\beta^2} \right], \quad (66)$$

where the plus sign is for $r_f > r_i$ and the minus sign otherwise. This form is consistent with the assumption of constant metric functions across zones (as is used in the actual code), but it can introduce difficulties when a trajectory moves from one zone to another near the radius of minimum propagation.

Clearly, equation 62 is a non-linear integro-differential equation due to the functional dependence of the scattering terms on the local distribution function. An approximate solution to the Lindquist equation is desired where the solutions along characteristics are decoupled and the formal solution can be directly integrated. The simplest approximation is to just to make the replacement $f \rightarrow f_{eq}$ in the scattering terms. This approximation will only be valid at high optical depth and is therefore suspect for use in the decoupling region. The next order approximation is to use a distribution function inferred from our knowledge of E_g and H_g . Assuming that the energy is distributed within a group as within a black-body gives

$$\begin{aligned} \hat{f}_0(\nu, r) &= f_{eq}(\nu, r) \frac{E_g}{B_g}, \\ \hat{f}_1(\nu, r) &= 3f_{eq}(\nu, r) \frac{H_g}{B_g}. \end{aligned} \quad (67)$$

Employing the Legendre expansion of the scattering kernel, integrating over outgoing neutrino angle, and only including the elastic scattering contribution gives the scattering source and sink terms

$$\begin{aligned} j_s(\omega, \mu) &= \frac{2\omega^2}{(2\pi)^2} \sum_{l=0}^{\infty} \frac{1}{2l+1} P_l(\mu) \tilde{R}_l^s(\omega) \hat{f}_l(\omega) \\ &\approx f_{eq}(\omega) \left\{ \chi_0^s(\omega) \frac{E_g}{B_g} + \mu \chi_1^s(\omega) \frac{H_g}{B_g} \right\} \end{aligned} \quad (68)$$

and

$$\lambda_s^{-1}(\omega, \mu) = \chi_0^s(\omega) - j_s(\omega, \mu). \quad (69)$$

Using the last characteristic equation, the solution of the linearized Boltzmann equation is

$$\begin{aligned} f(\nu, \beta, r_f) &= f(\nu, \beta, r_i) e^{-\tau(r_i, r_f)} \\ &+ e^{-\tau(r_i, r_f)} \int_{r_i}^{r_f} \frac{dr}{\Gamma\mu} e^{\tau(r_i, r)} \{j_s + f_{eq}/\lambda_a^*\} \end{aligned} \quad (70)$$

where the optical depth is

$$\tau(r_i, r_f) = \int_{r_i}^{r_f} \frac{dr}{\Gamma\mu} (1/\lambda_a^* + \chi_0^s). \quad (71)$$

This has the appealing property that there is no coupling between different β s and ν s, so the evolution of the distribution function along each path in phase space can be solved for independently.

4. NUMERICAL IMPLEMENTATION

Aside from the equation of state and neutrino opacities for dense matter, PNS evolution is described by the transport equations 28, 29, 30, 31, 32, and 33 and the structure equations 5, 6, 7, 3, and 8. These describe the evolution of the dependent variables $y(a, t) = \{r, u, m, \phi, n_B, T, Y_e, F_g, N_g, E_g, H_g\}$. To solve these equations numerically, the variables $\{a_{i+1/2}, r_{i+1/2}, u_{i+1/2}, m_{i+1/2}, F_{g,i+1/2}, H_{g,i+1/2}\}$ are discretized on zone edges while the variables $\{\phi_i, n_{B,i}, T_i, Y_{e,i}, N_{g,i}, E_{g,i}\}$ are discretized on zone centers. The derivatives in the PNS evolution equations are then finite differenced, turning them to algebraic equations for the above dependent variables. This is the most natural choice for discretizing the above equations, because the thermodynamic quantities, neutrino number density, and neutrino energy density are defined on zone centers while the neutrino number and energy fluxes are defined across zone edges which results in internal energy and lepton number conservation being made explicit in the discretized equations.

The general form of these algebraic equations is then

$$\mathcal{G}(y_{i-1}^{n,n+1}, y_i^{n,n+1}, y_{i+1}^{n,n+1}) = \mathcal{T}(y_i^n, y_i^{n+1}) + (1-\theta) \mathcal{Y}(y_{i-1}^n, y_i^n, y_{i+1}^n) + \theta \mathcal{Y}(y_{i-1}^{n+1}, y_i^{n+1}, y_{i+1}^{n+1}) \quad (72)$$

where n is the current time, at which the dependent variables are known, and $n+1$ is the next time step at which the dependent variables are desired. Here, \mathcal{T} denotes the differenced time derivatives and \mathcal{Y} denotes the rest of the terms. I choose to employ a fully implicit method for solving these equations, i.e. $\theta = 1$. This leaves a set of non-linear algebraic equations that must be solved to find the values of the dependent variables at time step $n+1$.

These equations are solved by standard high-dimensional Newton-Raphson (NR) techniques (Press et al. 1992). This requires calculating derivatives of all the functions g with respect to y . These derivatives are calculated analytically. Due to the number of derivatives, such an undertaking is prone to error. Therefore, all derivative functions are checked against numerical derivatives by automated software before they are included in the actual evolution code. The NR updates are given by the solution of an $N_z \times (6 + 2N_g N_s)$ -by- $N_z \times (6 + 2N_g N_s)$ matrix, where N_z is the number of radial zones, N_g is the number of neutrino energy groups, and N_s is the number of included neutrino species. This can rapidly become quite large for reasonable zoning and number of energy groups, and become too slow for dense matrix techniques. Luckily, the matrix involved is in fact block-diagonal, as each zone is only coupled to its neighboring zones, which significantly reduces computational time compared to solving a general dense matrix.

Although the equations are formally non-linear, they are sufficiently close to linear that NR iteration results in good convergence after a small number of iterations. It is generally demanded that the average relative deviation of the solution from zero is at least less than one part in a thousand. Often, the solution found by NR iteration satisfies the equations to close to machine precision. This scheme has been implemented using object-oriented FORTRAN2003. The block diagonal matrix

equations are solved using the software package **LAPACK** (Anderson et al. 1999).

To save computational time, the equations are solved using only the neutrino number equations and approximating the neutrino energy densities and fluxes using $E_g \approx \langle \omega \rangle_g N_g$. Once this set of equations is satisfied, a correction step is taken using the energy groups instead of the number groups. This approximation does not seem to introduce any significant error into the calculation. It is found that the total neutrino energy loss calculated using the approximation $E_g \approx \langle \omega \rangle_g N_g$ differs from the actual neutrino energy loss by around one part in a thousand when thirty energy groups are used. The code conserves lepton number to machine precision because lepton number conservation is explicitly enforced by equation 33. Conservation of total energy is not explicitly enforced. It is found that the total change in rest mass over the simulation agrees with the total neutrino energy lost to within a few percent. A series of test problems are performed with the code in Appendix A.

4.1. Equation of State

To close the transport and structure equations described above, an equation of state is required relating the pressure, energy density, and equilibrium neutrino chemical potential to n_B , T , and Y_e . Additionally, accurate derivatives of these quantities are required for calculation of the Jacobian matrix for NR iteration. Calls to the equation of state must also be computationally efficient. To meet these requirements, the equation of state is implemented in a tabular form. The Helmholtz free energy per baryon, $F = \epsilon - sT$, is tabulated as a function of n_B , T , and Y_e , as well as derivatives with respect to these variables up to second order. A bi-quintic interpolation is then used to get values of the free energy and its derivatives between grid points (Timmes & Swesty 2000). This guarantees that the thermodynamic functions will be smooth in the independent variables, thermodynamically consistent (Swesty 1996), and does not introduce problems in the calculation of the NR corrections.

The differential of the Helmholtz free energy is

$$\begin{aligned} dF &= -sdT + \frac{p}{n_B^2} dn_B + \sum_i \mu_i dY_i \\ &= -sdT + \frac{p}{n_B^2} dn_B + (\mu_e + \mu_p - \mu_n) dY_e. \end{aligned} \quad (73)$$

From this, the required thermodynamic quantities can be read off:

$$\begin{aligned} p &= n_B^2 \left(\frac{\partial F}{\partial n_B} \right)_{T, Y_e}, \quad s = - \left(\frac{\partial F}{\partial T} \right)_{n_B, Y_e}, \\ \text{and } \mu_{\nu_e, \text{eq}} &\equiv (\mu_e + \mu_p - \mu_n) = \left(\frac{\partial F}{\partial Y_e} \right)_{n_B, T}. \end{aligned} \quad (74)$$

4.2. Neutrino Opacities

The group averaged neutrino opacities are calculated using a ten point quadrature over each group to find an effective Planck mean opacity for the absorption terms in each group. The scattering and annihilation kernels which couple the groups, $\Phi_{g, g'}$, are calculated using a five point quadrature over both the incoming and outgoing

energies. Detailed balance is exploited to halve the number of calculations required. The scattering terms are not weighted by a local thermal neutrino distribution.

4.3. Integration of the Formal Solution

The formal solution to the static Boltzmann equation is calculated at the beginning of every time step and the Eddington factors enter the moment transport equations explicitly. Because time independent transport is assumed, no previous knowledge of the distribution functions is required and a new grid of impact parameters can be chosen at any time step, without having to worry about re-mapping old solutions as in Rampp & Janka (2002).

If all quantities are assumed to be constant across zones, the formal solution (equation 70) can easily be integrated, giving

$$f(\nu, \mu_s, r_{i+1/2}) = f(\nu, \mu_s, r_{i-1/2}) e^{-\Delta\tau_i} + \Delta f_0 + \Delta f_1 \quad (75)$$

for the change in f across zone i .

The physical path length across the zone, $\Delta\lambda_i$, is given by equation 66 and the optical depth across the zone is

$$\Delta\tau_i = \Delta\lambda_i (1/\lambda_a^* + \chi_0^s). \quad (76)$$

The additions to the neutrino beam from the medium and scattering from other beams are given by

$$\Delta f_0 = f_{\text{eq}} \frac{1/\lambda_a^* + \frac{E_g}{B_g} \chi_0^s}{1/\lambda_a^* + \chi_0^s} (1 - e^{-\Delta\tau_i}), \quad (77)$$

and

$$\Delta f_1 = f_{\text{eq}} \chi_1^s \frac{H_g}{B_g} e^{-\Delta\tau_i} \int_0^{\Delta\lambda_i} d\lambda \mu(\lambda) e^{\lambda(1/\lambda_a^* + \chi_0^s)}. \quad (78)$$

The integral required for Δf_1 cannot be calculated analytically because $\mu(\lambda)$ is a fairly complicated function. As this is a subdominant term, an ‘‘average’’ μ can be pulled out of the integral (which is allowable if μ does not change much across the zone). This gives the approximation

$$\Delta f_1 \approx \mu(r_i, \beta) f_{\text{eq}} \chi_1^s \frac{H_g}{B_g} \frac{1 - e^{-\Delta\tau_i}}{1/\lambda_a^* + 1/\lambda_s^*}. \quad (79)$$

Note that μ changes most rapidly when it is close to zero, but this term contributes the least in that region so the error from this approximation should not be too large.

Numerically, there is a problem with this formulation as it stands. Assume that a trajectory in zone i is close to its minimum radius of propagation, $\mu > 0$, and that it is close to a zone boundary. It then propagates to the zone boundary and is considered to be in zone $i + 1$. Because ϕ is increasing with radius, $\phi_{i+1} > \phi_i$. The new radius is taken to be $r_{L, i+1}$, so that the new angle of propagation is

$$\mu_n = \sqrt{1 - \left(\frac{r_m e^{\phi_{i+1} - \phi_i}}{r_{L, i+1}} \right)^2}, \quad (80)$$

$e^{\phi_{i+1} - \phi_i} > 1$, and $r_m \approx r_{L, i+1}$. Since, μ_n must be real, it becomes ill defined. In practice this problem is overcome setting μ to zero if it would have been imaginary.

Starting from the outer boundary of the computational grid, these equations are solved along an inward going

characteristic, through the radius of minimum propagation, and then along the outward going characteristic for each tangent ray. The impact parameters of the tangent ray grid are chosen to be equally spaced in radius for the calculations described in this paper. Once the distribution function for a particular energy at infinity has been calculated along tangent rays, moments of the distribution function at radii r_i are calculated from a weighted sum that reduces to the correct limit if the distribution function is locally constant in angle. Angular resolution is reduced at larger depths in the star. Because the distribution is extremely close to isotropy and $g_2 \approx g_3 \approx 0$, this does not pose a significant problem for PNS evolution.

4.4. Boundary Conditions

To close the system of transport equations, boundary conditions for the surface fluxes H_g and F_g are required. For this boundary condition, the formal solution is used to calculate the factors

$$\alpha_g = \frac{\int_{-1}^1 d\mu \mu f(r, \mu, \nu_g)}{\int_{-1}^1 d\mu f(r, \mu, \nu_g)}, \quad (81)$$

so that $F_{g,\text{bound}} = \alpha_g N_g$ and $H_{g,\text{bound}} = \alpha_g E_g$ in the final zone. At the inner edge of the computational grid, incident fluxes are specified (for PNS evolution, they are of course specified to be zero).

The boundary conditions for the radius, gravitational mass, velocity, and pressure are implemented by including a fixed ghost zone at the inner and outer boundaries. The boundary condition for the metric potential ϕ is given by matching to the Schwarzschild vacuum solution to the Einstein equations at the outer boundary. This gives $\phi_s = \log(\Gamma_s)$.

4.5. Rezoning

To maintain reasonable spatial resolution, conservative post time step re-gridding is employed. Where conservation laws do not specify the properties of a new zone, piecewise linear interpolation is used. This generally results in smooth radial dependence of the fluid quantities. The implementation is similar to the method used in *Kepler* (Weaver et al. 1978).

The re-gridding is driven by gradients in the density and radius. Generally, the radius is not allowed to vary by more than 5% between zones and the density is allowed to vary by no more than 20%. This generally results in approximately 100-150 zones being on the grid. The choice of relative density changes places high resolution in regions where neutrino decoupling is occurring.

4.6. Red Shifting Terms

Due to red and blue shifting between groups, equations 28, 29, 30 and 31 contain the un-integrated moments w^i . Therefore, an approximation method for these moments is required. When integrated over all energies, these terms go to zero. Therefore, any chosen numerical scheme must have terms balancing between groups for energy conservation. To move forward, something must be assumed about how energy is distributed in the groups. The simplest scheme is to assume that it is uniform. Then within a particular group

$w^{0,1} = \{N_g, F_g, E_g, H_g\}/(\omega_{g,H} - \omega_{g,L})$. It could also be assumed that the internal energy is distributed as a black body, which is consistent with the assumption used in the source terms. The uniform distribution is chosen due to its simplicity. For the H_g evolution equation, this results in

$$\begin{aligned} & -\omega_{g,U} \left[\left(\frac{\Theta}{3} + \frac{2}{5}\sigma + g_3 \frac{3}{2}\sigma - e^{-\phi} \frac{\partial \phi}{\partial t} \right) \left(\frac{H_g}{2\Delta\omega_g} + \frac{H_{g+1}}{2\Delta\omega_{g+1}} \right) \right] \\ & + \omega_{g,L} \left[\left(\frac{\Theta}{3} + \frac{2}{5}\sigma + g_3 \frac{3}{2}\sigma - e^{-\phi} \frac{\partial \phi}{\partial t} \right) \left(\frac{H_{g-1}}{2\Delta\omega_{g-1}} + \frac{H_g}{2\Delta\omega_g} \right) \right]. \end{aligned} \quad (82)$$

Similar expressions result for equations 28, 29, and 30. It is straight forward to verify that these terms disappear when summed over groups.

5. PROTO-NEUTRON STAR EVOLUTION

Rather than follow the collapse of a massive stellar core through bounce, the calculations here start from a separate calculation of the highly dynamic phase of initial collapse. For ease of comparison with previous work, the $1.6 M_\odot$ baryonic mass initial model from Pons *et al.* (1999) is employed and the affects of convection are not considered. This will correspond to a $1.4 M_\odot$ gravitational mass neutron star after it has cooled and can be thought of as representative of a standard neutron star (Kiziltan et al. 2010). The cooling and de-leptonization of this object is followed for 55 seconds, which is shortly after the time the PNS becomes optically thin.

5.1. Physical Ingredients

A relativistic mean field of equation of state consisting of only neutrons, protons, and electrons is assumed. The GM3 parameter set is used without hyperons (Glendenning & Moszkowski 1991), which is what was used in Pons *et al.* (1999). Neutrino opacities are also calculated in the relativistic mean field approximation using the formalism of Reddy et al. (1998). The tensor polarization is also included so that “weak magnetism” affects are included to all orders (Horowitz & Pérez-García 2003). The electron scattering rates from Yueh & Buchler (1977) are used for the inelastic scattering kernels. Nucleon scattering is assumed to occur within a single group, although the opacities are calculated using the full inelastic differential cross-sections. Bremsstrahlung is implemented using the structure function given in Hannestad & Raffelt (1998). Rather than include this in the annihilation kernels, the Bremsstrahlung mean free path has been calculated assuming a thermal distribution for the secondary neutrinos. Given the uncertainty in the Bremsstrahlung rate itself and its large density dependence, this is a reasonable approximation. Electron positron pair annihilation (Bruenn 1985) is also included. Pure neutrino processes (i.e. $\nu_e + \bar{\nu}_e \rightarrow \nu_\tau + \bar{\nu}_\tau$) are not included. This set of rates is fully consistent with the rate set used in Pons *et al.* (1999), but differs significantly from the rate sets used in recent collapse simulations (Hüdepohl et al. 2010; Fischer et al. 2011).

The study here uses 30 logarithmically spaced energy groups from 2 MeV to 75 MeV plus one final group extending from 75 MeV to 1000 MeV to encompass the tail of the thermal distribution. This final group is only

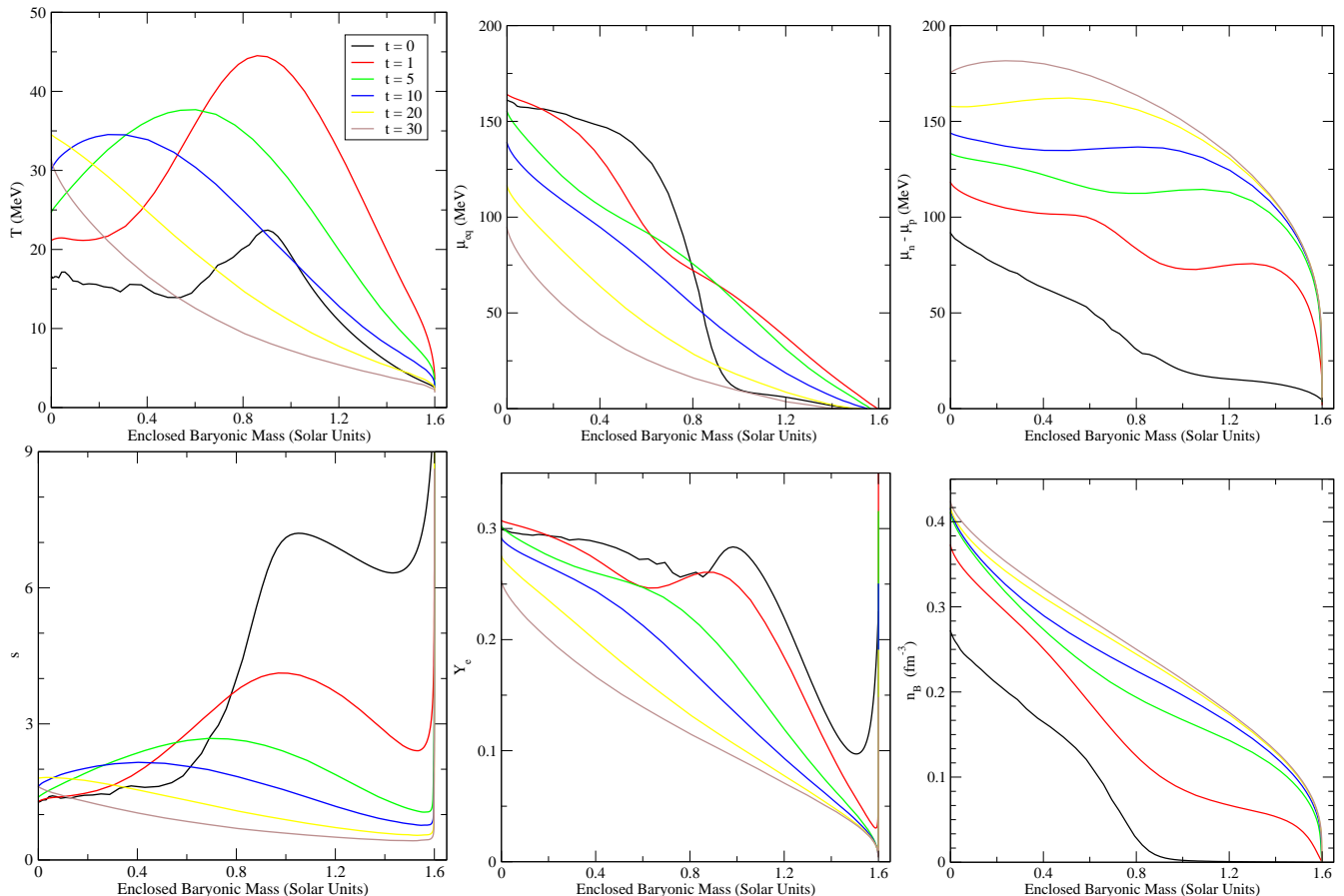


Figure 1. The internal structure of the PNS for selected times in the fiducial simulation. The temperature, equilibrium electron neutrino chemical potential, proton neutron chemical potential difference, dimensionless entropy per baryon, electron fraction, and baryon density are plotted at times 0 s, 1 s, 5 s, 10 s, 20 s, and 30 s, from left to right and top to bottom. The horizontal axes show the enclosed baryon number in units of the number of baryons in the sun ($N_\odot \equiv 12.04 \times 10^{56}$). This figure can be directly compared to figure 9 of Pons *et al.* (1999), as it was produced using the same initial model and a very similar nuclear equation of state and neutrino opacity set.

populated deep in the PNS and it is in tight thermal equilibrium due to the extremely short mean free paths for such high energy neutrinos. Minimal differences are found in the PNS evolution if only 20 groups are employed to cover the same energy range.

The adaptive radial gridding algorithm is set to keep approximately 130 zones on the grid and allow for at most a 20% change in density across a zone and a 10% change in radius across a zone. The boundary pressure is set so that the outer edge of the model has a density around $2 \times 10^9 \text{ g cm}^{-3}$. This is a sufficiently low density that all of the neutrinos have decoupled well within the outer boundary.

5.2. Structural Evolution

Qualitatively, the internal structure of the PNS evolution follows the standard picture of Kelvin-Helmholtz PNS cooling as described by Burrows & Lattimer (1986), Keil & Janka (1995), and Pons *et al.* (1999), where the gravitational binding energy of the compact object provides energy lost to neutrino emission. After the shock produced by the supra-nuclear density bounce of the core propagates through the outer layers of the PNS, a high entropy shocked region is left on top of a cold un-shocked PNS core, which has an entropy similar to the initial entropy of the pre-supernova iron core. The outer shocked

layers have de-leptonized during the ν_e burst, but neutrinos in the core itself have been trapped since before bounce (although partial deleptonization has occurred), resulting in a large non-zero $\mu_{\nu_e, \text{eq}}$ and $Y_e \approx 0.3$ (c.f. Liebendörfer *et al.* 2001b). This provides the initial condition for PNS cooling.

The internal structure of the PNS simulation is shown in figure 1 for a number of times (with time zero corresponding to the starting point of the simulations, not the time of core-bounce). The models start with a core entropy of ~ 1.2 . The entropy rises from 1.6 at an enclosed baryonic mass of $\sim 0.6 M_\odot$ to 7.4 at an enclosed mass of $1.0 M_\odot$. This implies that the supernova shock was born at around $0.6 M_\odot$, which is reasonably consistent with the core-collapse results of Thompson *et al.* (2003). The shocked mantle is at low density relative to the core and extends to large radius (material that is at a density of 10^{-5} fm^{-3} is found at 99 km), mainly due to the thermal contribution to the pressure.

From this initial state, the shock heated mantle rapidly contracts over the first second or so of the simulation. This contraction is driven by the rapid loss of energy and lepton number via neutrinos, which can readily escape due to the low density of the envelope and long interaction mean free paths. The loss of lepton num-

ber and thermal energy reduces pressure support in the mantle, and the mantle responds by rapidly contracting (i.e., rapid relative to the cooling timescale of the core, not rapid compared to the dynamical timescale of the envelope). By two seconds into the simulation, material at a density of 10^{-5} fm^{-3} is at 17 km. This is fairly close to the cold neutron star radius for GM3 (13.5 km). The work provided by this contraction is enough to increase the peak temperature of the mantle from 22 MeV to 45 MeV even though the entropy of the mantle has decreased from 7 to 4 over this period.

This period of the PNS evolution is most likely to be sensitive to the initial conditions for the simulations, as at later times the details of the initial structure should be washed out. The envelope of the PNS should also be convective, which significantly alters the rate of energy and lepton number transport in the PNS (c.f. Roberts et al. 2012). Additionally, there might be significant accretion luminosity over this period (although this is approximately accounted for by the mantle). Therefore, especially given the older provenance of the initial conditions, the results from this period should be taken as only qualitatively correct.

While the mantle is contracting, $\bar{\nu}_e$ s and ν_x s are being transported down the positive radial temperature gradient into the core while the ν_e s are being transported outwards down the large equilibrium chemical potential gradient. This results in a net heat flux into the core and a net lepton flux out of the core. This has been referred to as “Joule heating” of the core in previous work (Burrows & Lattimer 1986). Additionally, the inner regions contract over this period due to the increased boundary pressure on the un-shocked core from the cooling mantle. This contributes to the temperature increase in the core in addition to the Joule heating.

After the initial period of mantle contraction, the density structure of the PNS becomes similar to that of a cold PNS. Joule heating continues to increase the temperature of the inner most regions until the central temperature reaches its peak value of 35 MeV at 18 s in the simulation. Then, the temperature of the entire star falls with time. The entropy evolution exhibits a similar behavior. Lepton number is lost from the entire PNS core over this time and the electron fraction evolves toward the expected value for matter in beta-equilibrium with no net electron neutrino number. After about 15 seconds, contraction slows since the PNS is nearly at the cold neutron star radius. After this, neutrino emission is powered chiefly by the loss of thermal energy from the star.

It is also worth noting that the temperature gradient and the $\mu_{\nu_e, \text{eq}}$ gradient in the shocked layers of the PNS become increasingly shallow from 1 s onwards. Additionally, as the density of the outer layers rises, the neutron proton chemical potential difference $\hat{\mu} = \mu_n - \mu_p$ gets larger. The increase in $\hat{\mu}$ and the decrease in $\mu_{\nu_e, \text{eq}}$ bring $\hat{\mu}$ close to the electron chemical potential $\mu_e = \hat{\mu} + \mu_{\nu_e, \text{eq}}$ as time goes on. These considerations have significant consequences for the spectral evolution of the neutrinos and which are discussed in section 6.2.

5.3. Emergent Luminosity and Spectral Evolution

The total integrated energy loss in neutrinos over the duration of the simulation is $E_\nu = 2.32 \times 10^{53} \text{ erg}$, and

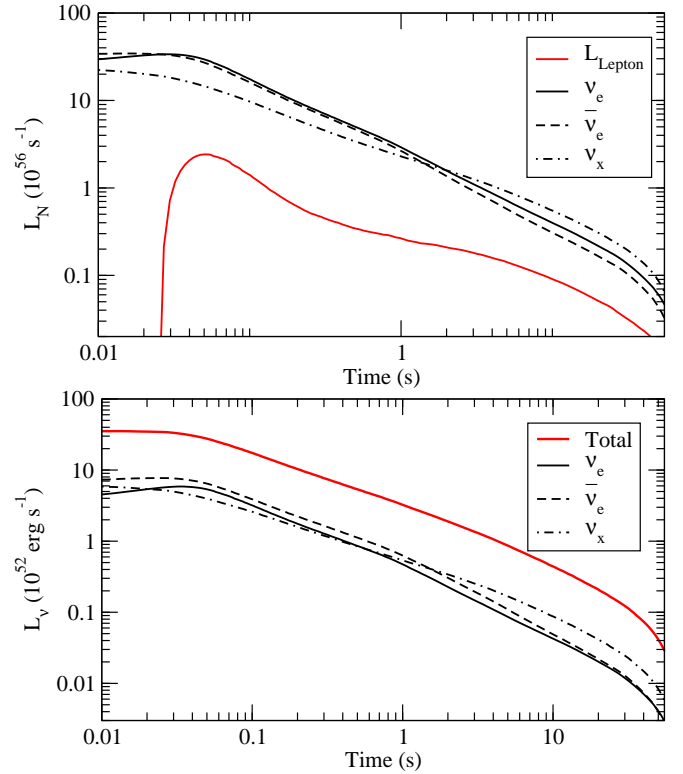


Figure 2. Top panel: Number luminosities as a function of time for ν_e (solid black line), $\bar{\nu}_e$ (dashed black line), ν_x (dot-dashed black line) and the de-leptonization rate, $\dot{N}_{\nu_e} - \dot{N}_{\bar{\nu}_e}$. Bottom panel: Energy luminosities as a function of time. The black lines are the same as in the top panel, but the solid red line is the total energy emitted in neutrinos per time.

the total lepton number radiated is $N_L = 3.2 \times 10^{56}$. The neutrino emission from the PNS is shown in figure 2. As is discussed above, the first couple of seconds are dominated by the contraction of the PNS mantle. Over the first second of the simulation, 38% of the total neutrino energy loss and 20% of the total lepton number loss occurs. During this period, the ν_x number luminosity is produced mainly by the un-shocked core, as the μ and τ neutrinos are mainly coupled to the envelope through scattering. Therefore, the luminosity in these flavors is lower because of the smaller emitting surface (which is not offset by the temperature of the core).

During mantle contraction, there is a high de-leptonization rate driven by the outermost layers of the star. After the first few hundred milliseconds, de-leptonization slows as the outer layers go towards $\mu_{\nu_e, \text{eq}} \approx 0$ and de-leptonization is driven by diffusion out of the core. The values of the de-leptonization rate before 80 ms are unrealistic, as they are determined by the relaxation of the assumed initial conditions for the neutrinos.

Over the first two seconds, the ν_x luminosities are significantly lower than the luminosities of the electron flavored neutrinos. The neutrino energy and number luminosities as a function of radius at 500 ms after the beginning of the simulation are shown in figure 3. First, this illustrates that the μ and τ neutrino number fluxes are being set much further inside the star (at around 18

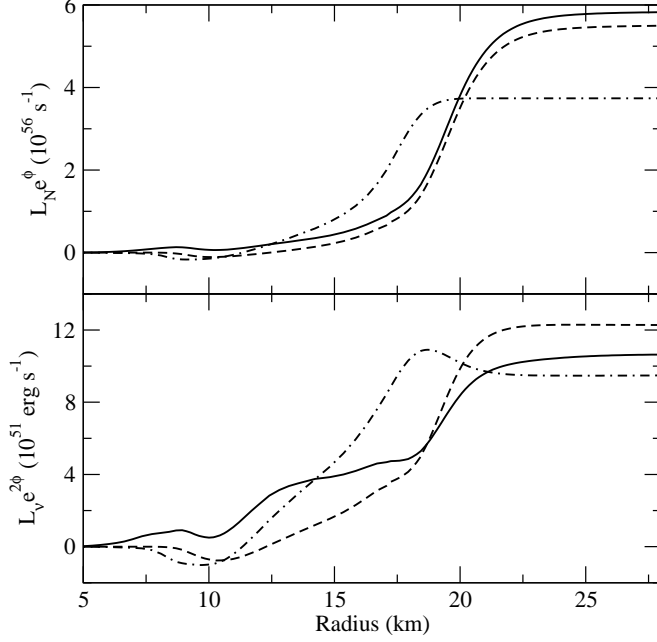


Figure 3. Neutrino number and energy luminosities at infinity as a function of radius at 500 ms into the simulation. The solid lines are for electron neutrinos, the dashed lines are for electron antineutrinos, and the dot-dashed lines are for μ and τ neutrinos.

km) than the electron neutrinos, but they exchange energy out to a significantly larger radius via scattering. Second, there is an inward directed anti-electron, μ and τ flux near the mantle core boundary. As cooling precedes, heat diffuses down the positive temperature gradient (and positive equilibrium chemical potential gradient for the anti-electron neutrinos) into the lower entropy core. This is the Joule heating discussed above. In contrast, the large negative equilibrium chemical potential gradient for the electron neutrinos overwhelms the positive radial temperature gradient and the electron neutrino flux is positive everywhere.

After the PNS has contracted to close to the cold neutron star radius, the ν_x luminosity has increased relative to the ν_e and $\bar{\nu}_e$ luminosities. In fact, the ν_x luminosity is about twice the luminosity in either of the electron neutrino species. These neutrinos decouple further inside the PNS and are therefore emitted at a higher effective temperature, resulting in a larger number and energy luminosity. Between thirty and forty seconds the PNS becomes transparent to neutrinos and the luminosity drops off significantly.

The average energies of the emitted neutrinos at infinity as a function of time are shown in figure 4. Within the integrated energy group formalism, the neutrino energy moments at infinity are defined as

$$\langle \epsilon^n \rangle = e^{n\phi_s} \frac{\sum_g \langle \omega \rangle_g^{n-1} H_g}{\sum_g F_g}, \quad (83)$$

where $\langle \omega \rangle_g$ is a group averaged energy and ϕ_s is the surface value of the metric potential.

During the mantle contraction phase, there is the standard hierarchy of neutrino average energies $\langle \epsilon_{\nu_e} \rangle < \langle \epsilon_{\bar{\nu}_e} \rangle < \langle \epsilon_{\nu_x} \rangle$. After mantle contraction has ceased, the

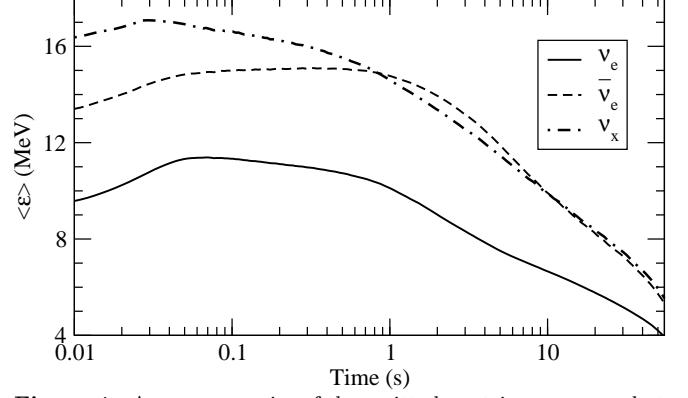


Figure 4. Average energies of the emitted neutrinos measured at infinity.

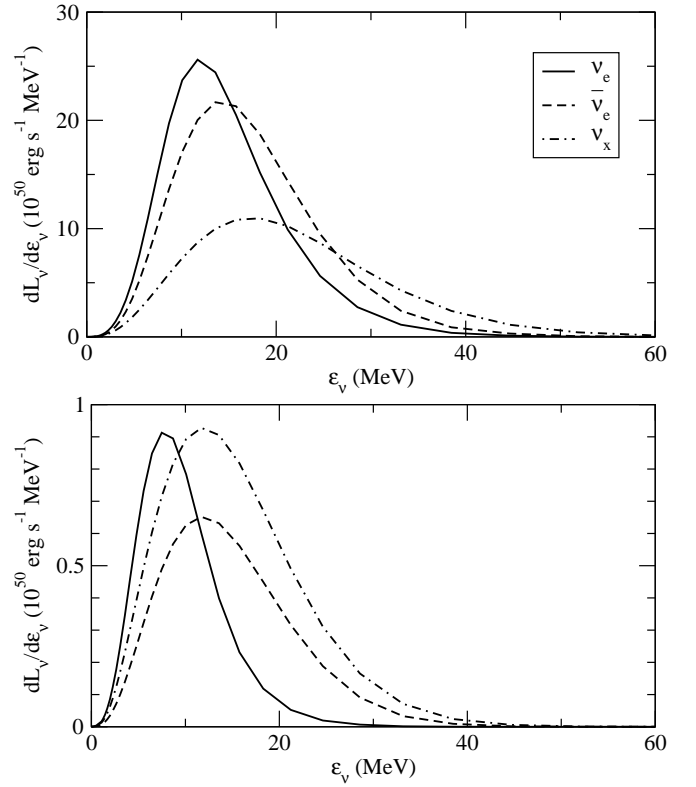


Figure 5. Neutrino spectra for all three flavors tracked in the simulation. The top panel is at 100 ms after the start of the simulation, the bottom panel is the spectrum at 5 seconds.

energy decoupling radius of electron neutrinos and μ and τ neutrinos becomes similar and for the rest of the PNS evolution $\langle \epsilon_{\bar{\nu}_e} \rangle \approx \langle \epsilon_{\nu_x} \rangle$. This is in contrast to the difference between the electron neutrino and anti-neutrino average energies, which obey $\langle \epsilon_{\nu_e} \rangle < \langle \epsilon_{\bar{\nu}_e} \rangle$ for the entire calculation, although the two average energies get closer at late times. An analysis of why this is, its implications, and a comparison to other results in the literature is given in section 6.2.

The emitted neutrino spectra at two representative times are shown in 5 for reference. The ν_x neutrinos decouple further in the star than the $\bar{\nu}_e$ neutrinos at five seconds into the simulation so that they have a larger

number luminosity due to the larger temperatures found there, but these flavors have a similar energy sphere due to inelastic scattering which accounts for the similar value of the peak of the luminosity as a function of neutrino energy.

6. DISCUSSION

6.1. Comparison to EFLD

Until recently (Hüdepohl *et al.* 2010; Fischer *et al.* 2010), most studies of PNS cooling used the EFLD approximation to describe neutrino transport (Burrows & Lattimer 1986; Keil & Janka 1995; Pons *et al.* 1999; Roberts *et al.* 2012). It is thus a worthwhile exercise to compare the results obtained using EFLD and the present variable Eddington factor method for transport. No detailed comparison of the effect of different flux limiters is attempted since EFLD clearly breaks down in the decoupling regime independent of the flux limiter used. See Messer *et al.* (1998) and Pons *et al.* (2000) for discussions of the affect of different flux limiters.

Models using the identical microphysics and initial conditions described in section 5 were calculated using the EFLD code described in Roberts *et al.* (2012) with convection turned off. This code is similar to the one used in Pons *et al.* (1999) and is completely different from the one used in this paper. A derivation of EFLD in the context of this paper is included in Appendix B. The EFLD luminosities as a function of time are shown in figure 6, alongside the luminosities from section 5. EFLD clearly does a reasonably good job of predicting the total neutrino luminosity, but poorly predicts the luminosities of each flavor.

At early times, some deviation in the total luminosity is expected because the mantle, which is driving most of the neutrino emission, is not particularly optically thick. Additionally, at late times when the whole PNS becomes optically thin, EFLD deviates from the variable Eddington factor solution. But for the bulk of the PNS evolution the deviation between the two methods is around 10%, which is surprisingly good agreement. Given that most predictions made using EFLD codes have relied only on the total neutrino luminosity, it seems that previous results can be reasonably trusted. The total luminosity emitted from the PNS is set at the neutrino spheres of each flavor, which is the last point at which EFLD can be considered reliable. The outermost layers of the PNS in which the neutrinos decouple can come into radiative equilibrium on a short timescale and therefore rapidly adjust to the flux being pushed through them from below. As neutrinos propagate through the outer layers in the EFLD formalism, flux may be shifted between flavors unrealistically but the outer layers of the PNS will rapidly evolve to carry the right total luminosity. Therefore, it is not surprising that EFLD gets the total luminosity right but fails to predict the luminosities of specific flavors. Of course, EFLD makes no predictions regarding the spectral properties of the neutrinos.

6.2. Neutrino Spectra and The Composition of The Neutrino Driven Wind

The most striking difference between the present simulations and other recent studies (Hüdepohl *et al.* 2010;

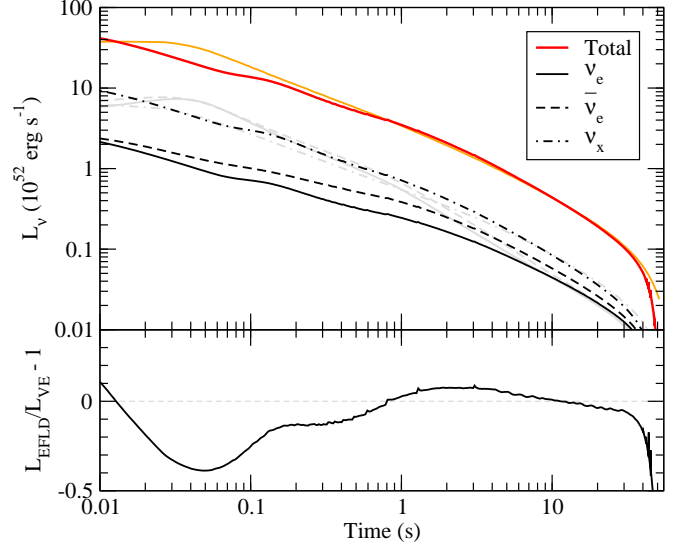


Figure 6. Luminosities as a function of time for ν_e (solid black line), $\bar{\nu}_e$ (dashed black line), ν_x (dot-dashed black line) of time and the total luminosity (red line) in the EFLD approximation. The gray and orange lines is the data from figure 2. The bottom panel shows the ratio of the total EFLD luminosity to the total luminosity calculated using the new code.

Fischer *et al.* 2010) is the greater difference in the present study of the electron neutrino and anti-neutrino average energies at late times. There are a number of possible reasons for this difference.

One is the initial model chosen for the PNS evolution. Rather than use an initial model from a separate calculation of core-collapse, both Hüdepohl *et al.* (2010) and Fischer *et al.* (2010) follow the entire evolution of the supernova. In so far as the initial models are similar, the two approaches should give the same answer. The initial model used here is somewhat dated and was chosen mainly to facilitate the comparison with the work of Pons *et al.* (1999). At early times the initial progenitor model will certainly affect the properties of the emitted neutrinos significantly, but after the first second Pons *et al.* (1999) found that the evolution does not depend sensitively on the initial progenitor model. Of course, the difference in the average energies of the electron and anti-electron neutrinos is a fairly subtle effect. Therefore, the effect of the progenitor model should not be ruled out, but based on the argument below it seems unlikely that the progenitor model is the dominant factor.

It is possible that the methods used for transport differ enough to give disparate results. This also seems unlikely considering all three approaches come close to directly solving the Boltzmann equation, that the formalism described in this work is fairly similar to the formalism of Hüdepohl *et al.* (2010) (see Rampp & Janka 2002), and that the approaches of Fischer *et al.* (2010) and Hüdepohl *et al.* (2010) have been shown to yield similar results (Liebendörfer *et al.* 2005).

A more significant difference though may be the microphysics employed. The difference between the electron neutrino and anti-neutrino spectral temperatures is mainly set by the difference between their respective

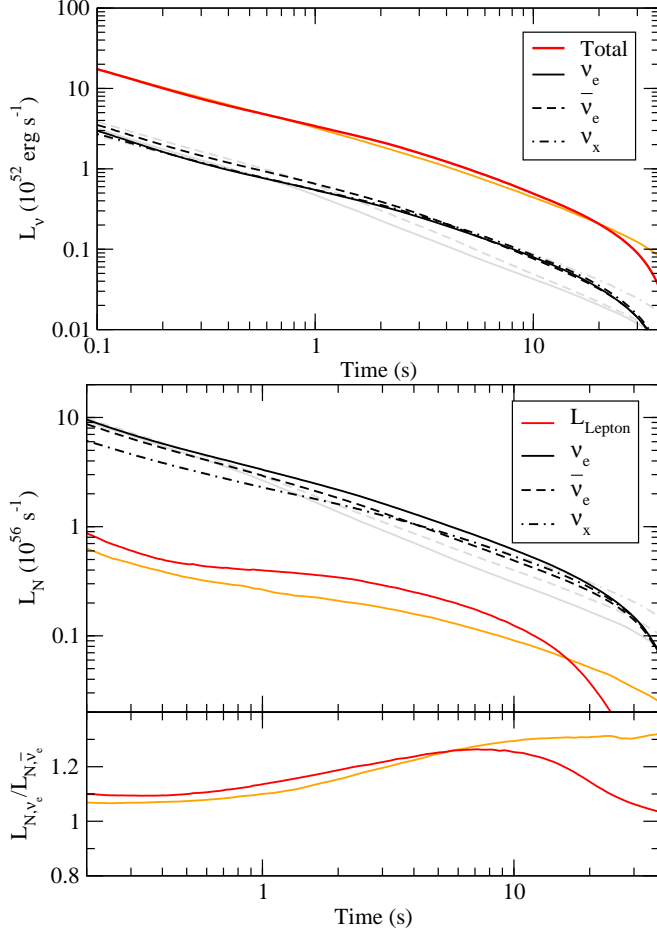


Figure 7. Energy and number luminosities for a model using the Bruenn (1985) nucleon capture rates compared to the fiducial model described in section 5. Notice the slightly increased ν_e and $\bar{\nu}_e$ cooling rates at late times and the convergence of all three luminosities. The black lines and red lines are for the model using Bruenn (1985) rates, while the gray and orange lines are for the model described in section 5. In the bottom plot, the ratio $N_{\nu_e}/N_{\bar{\nu}_e}$, which is of consequence to the electron fraction in the neutrino driven wind, is shown in the bottom plot of the second panel.

mean free paths to capture on nucleons, as the scattering mean free paths for both species are nearly equal. Due to de-leptonization, there are far more neutrons to capture electron neutrinos than protons to capture electron anti-neutrinos. Of course, it is possible for both of these reactions to have strong final state blocking (electron blocking for the neutrinos and neutron blocking for the anti-neutrinos). If it is assumed that there is no energy transfer to the nucleons, as in Fischer et al. (2011), then both reactions will be strongly blocked, the elastic interaction rates described in Bruenn (1985) go to the same value, and it is expected that average electron neutrino and anti-neutrino energies will be similar at late times due to the similar charged current mean free paths for both species.

The final state blocking symmetry predicted by the charged current rates of Bruenn (1985) does not agree with more detailed calculations of the electron neutrino capture rates. There is in fact a strong asymmetry between the two reactions, because there is signifi-

cantly more energy available in the entrance channel for $\nu_e + n \rightarrow e^- + p$ than for $\bar{\nu}_e + p \rightarrow e^+ + n$. The difference between the energy of the entrance channels is just the difference between the Fermi energies of the neutrons and protons. The Fermi energies for interacting nucleons are given by $e_{F,i} = k_{F,i}^2/2M_i + U_i$, where U_i is an isospin dependent potential energy due to strong interactions in the medium. For neutron rich conditions, the neutron potential energy is larger than the proton potential energy due to the nuclear symmetry energy. Most of the potential difference, $U_N - U_P$ is transferred to the outgoing electron in the reaction $\nu_e + n \rightarrow e^- + p$. This effect can significantly decrease the absorption mean free path for electron neutrinos. Due to the large value of the nuclear symmetry energy relative to the value expected for free nucleons, $U_N - U_P$ accounts for a significant fraction of $\bar{\mu}$. Although this amount of energy is often not enough to put the final state electron above the electron Fermi surface, it is enough to put the final state electron in a relatively less blocked portion of phase space. This effect is included in the relativistic formalism of Reddy et al. (1998), which is used to calculate the neutrino interaction rates used in the models presented in this work. The details of the importance of realistic kinematics on charged current rates will be discussed in future work.

To illustrate how more realistic rates affect the predicted neutrino properties, a model identical to the one described in section 5 was run, except that the nucleon capture rates were replaced with the Bruenn (1985) capture rates neglecting the nucleon potentials. The luminosities as a function of time are shown in figure 7. The changes in the luminosity are relatively small. The most obvious difference is that the luminosities of all neutrino species asymptote to one another at late times, which is similar to the behavior seen in Fischer et al. (2011). From one to ten seconds, there is a significantly smaller difference between the luminosities than in the fiducial model. Cooling via electron neutrinos and anti-neutrinos is also increased at late times, but the ν_x luminosity is virtually unchanged, as expected. Before 1 s, the electron neutrino luminosity is reduced. It is unlikely that this is significant, as the first approximately hundred milliseconds of these simulations are suspect for the reasons described above. The reason for the early time decrease is less clear. It is unlikely that this is due to the effects of nuclear interactions because the region where electron neutrinos decouple is in the mantle which is at low density.

The evolution of the average neutrino energies are shown in figure 8. There is little change between the models in the electron anti-neutrino, μ , and τ neutrino average energies, but there is a significant change in the electron neutrino average energies. At early times the average energy is reduced compared to the fiducial model and at late times it is increased. The late-time convergence is easily explained by the argument given in the paragraphs above and by the arguments given in Fischer et al. (2011).

This difference is important to the composition of the neutrino driven wind. The electron fraction of the neutrino driven wind can be estimated as (Qian & Woosley

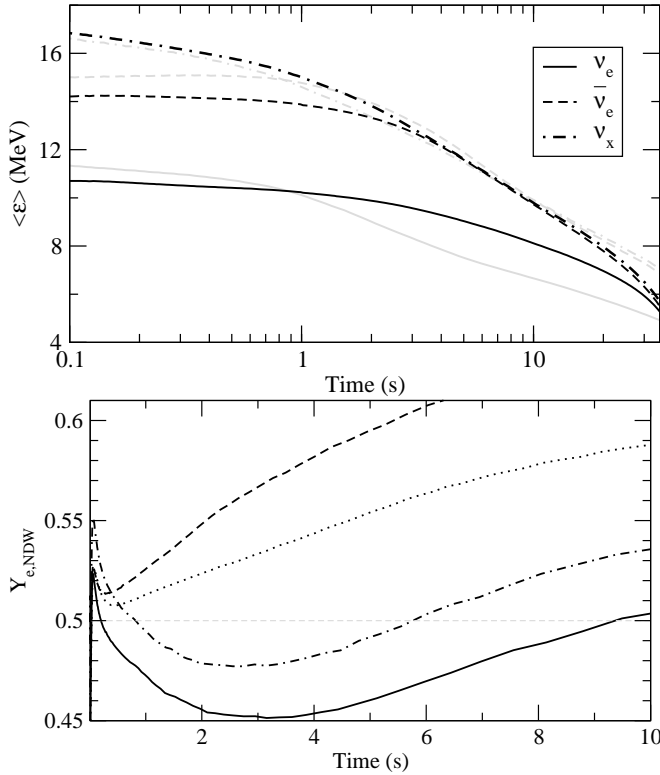


Figure 8. Top panel: Energy moments of the outgoing neutrino flux measured at the surface of the calculation using the Bruenn (1985) approximation for the electron neutrino and anti-neutrino capture rates on nucleons (black lines). The gray lines are for the fiducial model using the full capture cross-sections from Reddy et al. (1998). There is little variation for the $\bar{\nu}_e$ and ν_x energies between the two cross-section prescriptions, but there is a significant change in the ν_e average energies. Bottom panel: Predicted neutrino driven wind electron fraction as a function of time. The dotted line is from a PNS model using the Bruenn (1985) rates, the solid line is for the Reddy et al. (1998) rates including tensor polarization corrections and the mean fields (Horowitz & Pérez-García 2003), the dot-dashed line is a model using the Reddy et al. (1998) rates without tensor polarization corrections and with mean fields, and the dashed line is a model using the Reddy et al. (1998) rates with tensor polarization corrections but neglecting the effects of mean fields. Note that neutron richness is predicted from about 1.5 to 10 seconds when realistic kinematics is used in the capture rates, while the wind is predicted to be proton rich throughout when the effects of the neutron and proton potentials are ignored.

1996)

$$Y_{e,\text{NDW}} \approx \left[1 + \frac{\dot{N}_{\bar{\nu}_e} \langle \sigma(\epsilon)_{p,\bar{\nu}_e} \rangle}{\dot{N}_{\nu_e} \langle \sigma(\epsilon)_{n,\nu_e} \rangle} \right]^{-1} \quad (84)$$

where $\langle \sigma \rangle$ are the energy averaged cross-sections for neutrino capture on nucleons, which are approximately proportional to ϵ^2 . Smaller relative ν_e average energies and lower de-leptonization rates lead to a lower electron fraction in the wind.

The evolution of the electron fraction in the neutrino driven wind calculated using equation 84 for both models, as well as a model that does not include weak magnetism corrections and a model that does not include mean field effects, but which do include full kinematics in the structure functions, is shown in the second panel of figure 8. The capture rates for low densities given in Burrows et al. (2006), which include first order

weak magnetism and recoil corrections, have been used. This was done to put the comparison between the models on even footing, although it is not necessarily consistent with the rates used inside the PNS itself. The alpha effect (Fuller & Meyer 1995) has also not been taken into account, which will push Y_e closer to a half in both proton and neutron rich conditions. Energy moments of the neutrino flux are taken using the values at the surface of the computational domain, not at infinity. The $\dot{N}_{\nu_e}/\dot{N}_{\bar{\nu}_e}$ term is increasing with time in both models (see figure 7), which increases the electron fraction in the wind. Note that once neutrinos are free streaming, this term is invariant with radius.

With these assumptions, the fiducial model of section 5 actually does result in a period of neutron richness in the wind, in contrast to the results of Hüpdepohl *et al.* (2010) and Fischer et al. (2011). The wind is not very neutron rich ($Y_e \gtrsim 0.45$ at all times) and this change, by itself, would not result in substantial r -process nucleosynthesis in the standard neutrino driven wind where entropies are $\lesssim 150$ (Roberts et al. 2010). If for some reason the entropy were higher though, the possibility of an r -process remains. In contrast, the model that uses the rates of Bruenn (1985) and the model using the Reddy et al. (1998) rates without isospin dependent nuclear potentials consistent with the underlying equation of state results in a wind that is always proton-rich.

To emphasize that this result is mainly due to the reaction kinematics and not the inclusion of weak magnetism, models with the tensor polarization set to zero are also shown in the bottom panel of figure 8. As is expected from the first order weak magnetism corrections given in Horowitz (2002), allowing for a tensor portion of the response increase the difference between the electron neutrino and anti-neutrino average energies. This results in a lower electron fraction in the case including the tensor polarization relative to the case without. Still, the change between these two models is only a fraction of the change in the electron fraction when the Bruenn (1985) rates are used.

Given the sensitivity to the neutrino interaction rates, it is possible that further improvement of the treatment of electron neutrino and anti-neutrino capture will alter this conclusion in one direction or the other. Because the asymmetry between the electron neutrino capture rates depends on the value of the symmetry energy and the symmetry energy varies with density (Fattoyev *et al.* 2010), it may be that different nuclear equations of state alter the predicted neutron excess in the NDW. Variations of the calculation of the rates, such as incorporating the effect of correlations in the nuclear medium, can significantly change the timescale of the neutrino emission (Reddy *et al.* 1999) and possibly the spectral properties. Even if updated rates only change the rates at high density, this may affect $\dot{N}_{\nu_e}/\dot{N}_{\bar{\nu}_e}$ and thereby change the properties of the wind. Such extensions depend on the underlying equation of state, which is uncertain, and also on approximations inherent to many-body theories of strongly interacting systems. While this deserves further consideration, the results presented here seem to indicate that effects due to kinematics, degeneracy and mean fields are crucial.

It bears mentioning that the study of Hüpdepohl *et al.* (2010) did allow for energy and momentum transfer be-

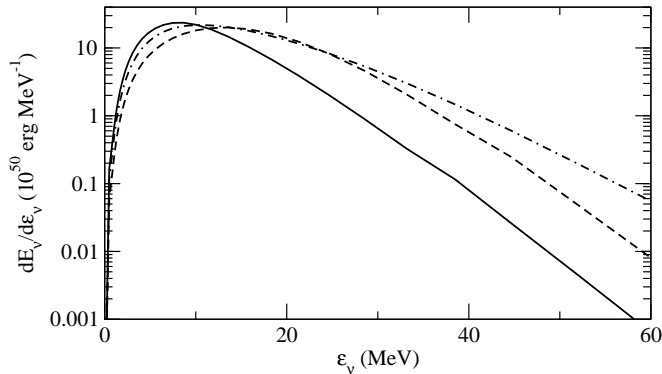


Figure 9. Spectrum of integrated neutrino emission over the duration of the simulation. Although the peak of the $\bar{\nu}_e$ spectrum corresponds to the peak of the ν_x spectrum, the ν_x spectrum has a significantly harder tail.

tween the nucleons and leptons (Buras et al. 2006), but did not account for the difference between the neutron and proton mean field potentials. Their rates were calculated within the random phase approximation of Burrows & Sawyer (1999), which is an improvement over the mean field rates used in this work. Additionally, weak magnetism corrections were approximately included in this study via the prescription of Buras et al. (2006). Their average energies were further apart than when the Bruenn (1985) rates were used, but the difference was still not great enough to result in a wind with a neutron excess. The average energies of the electron neutrinos and anti-neutrinos also asymptote to one another fairly rapidly in Hüdepohl *et al.* (2010), in contrast to the present study. This is all reasonably consistent with the affect of neglecting the mean field potentials in the nucleon kinematics, but it is far from certain that this is the main source of discrepancy. Further exploration of why this work differs from the work of Hüdepohl *et al.* (2010) is surely warranted.

Even given these caveats, it is tantalizing that the wind is neutron rich in the fiducial model once again. Extensions of the standard neutrino driven wind model which include heating from a source besides neutrinos can produce the r -process even for such modest neutron excesses (Suzuki et al. 2006).

6.3. Time Integrated Spectra

In figure 9, the integrated neutrino luminosity as a function of neutrino energy at infinity is shown for the model described in section 5. The time integrated average energies of the neutrinos are $\langle \epsilon_{\nu_e} \rangle = 8.3$ MeV, $\langle \epsilon_{\bar{\nu}_e} \rangle = 12.2$ MeV, and $\langle \epsilon_{\nu_x} \rangle = 11.1$ MeV. Although the μ and τ neutrinos are as hot or hotter than the electron anti-neutrinos at early times, the time integrated average is weighted more strongly towards late times so that they in fact have a somewhat lower average energy.

Time integrated neutrino spectra are interesting for both nucleosynthesis via the ν -process (Heger et al. 2005) and for predictions of the diffuse supernova neutrino background (Ando 2004). The neutrinos are non-thermal and are not easily described by an effective Fermi-Dirac distribution. Given the sensitivity of the ν -process to the energy of the emitted neutrinos (especially the energies above threshold), it seems that calcu-

lations of neutrino-induced nucleosynthesis needs to be done with more accurate neutrino spectra to check previous results in the literature. These integrated spectra are only approximate however because a substantial fraction (20%) of the neutrinos are emitted during the first second of mantle contraction, this phase of evolution contributes the majority of the high-energy tail, and the mantle contraction phase is most sensitive to the approximate initial conditions used.

7. CONCLUSIONS

A new code for following the evolution of PNSs has been described and some first results obtained. In section 2.2, a formalism for moment based neutrino transfer with variable Eddington factors has been described, based on the work of Thorne (1981) and Lindquist (1966). The framework is fully general relativistic and is formulated in the rest frame of the fluid, which simplifies calculation of the collision terms. The code employs energy integrated groups, rather than discrete energies, for solving the radiative transfer problem. This makes it well suited for dealing with problems where thermodynamic equilibrium holds in large portions of the problem domain and the distribution functions may contain sharp Fermi surfaces. A method for finding Eddington factors from a formal solution to the static Lindquist equation was also described. Additionally, general descriptions of the source terms for absorption, scattering, and pair annihilation have been provided which are consistent with the formalism, explicitly obey detailed balance, and therefore naturally deal with the transition to equilibrium. The details of a fully implicit numerical implementation of these transport equations alongside the equations of general relativistic hydrodynamics were then described in section 4.

The results of a fiducial model of PNS cooling were presented in section 5. The evolution proceeds similarly to previous results in the literature in which a similar nuclear equation of state and neutrino opacities were used. I have focused on the spectral properties of the emitted neutrinos, which were not well described by the formalism of Pons *et al.* (1999). Similar behavior is found to other recent results in the literature: spectral softening as a function of time and convergence of the $\bar{\nu}_e$ and $\nu_{\tau,\mu}$ luminosities after about two seconds of evolution (Fischer *et al.* 2010; Hüdepohl *et al.* 2010).

In contrast to other recent studies (c.f. Fischer et al. 2011) however, the new studies show that the average energy of the electron neutrinos does not converge to the average energies of the other neutrino flavors at late times. Additionally, the electron neutrinos are significantly cooler than the anti-electron neutrinos for most of the simulation. This difference is likely due to the treatment of charged current neutrino interactions, where a realistic treatment of the nucleon kinematics including the nuclear potential is important (see section 6.2). The implications of this result for the electron fraction in the neutrino driven wind and possible r -process nucleosynthesis in this environment were discussed and warrant further exploration.

A quantitative comparison was also made between the results of an EFLD calculation of PNS evolution and evolution with the code described in this paper in section 6.1. It was found that EFLD provides a good approximation

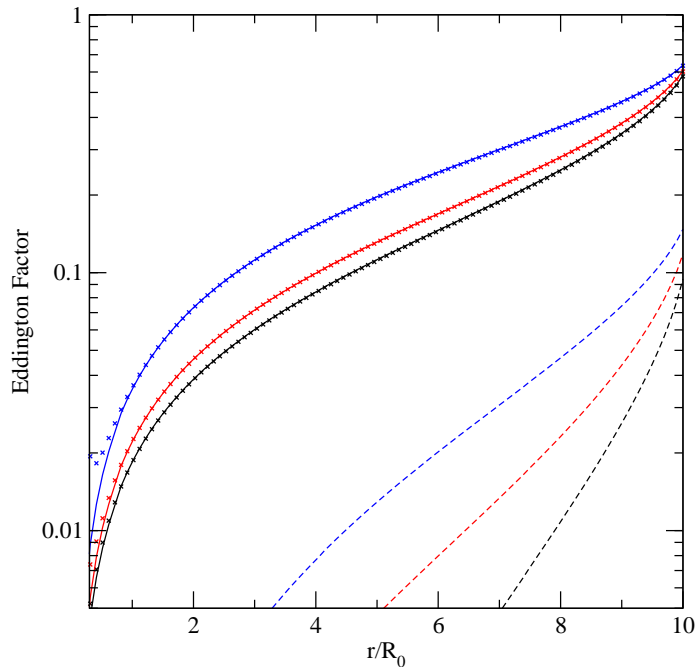


Figure 10. Comparison of H_g/E_g (crosses) and g_1 (solid lines) for a purely absorbing (black lines) and an isotropic scattering sphere (red lines) with total optical depth one and a first order scattering sphere (blue lines) with $\tau = 0.1$. Aside from at the center, there is excellent agreement between the formal solution and the results of the moment calculation. The dashed lines are the second Eddington factors, g_2 , for the same models.

to the total neutrino luminosity during periods in which the neutrino luminosity is dominated by emission from optically thick regions. This approximation does break down in the optically thin regime as expected. Additionally, it does a poor job of predicting the luminosities of individual neutrino flavors.

The most significant improvement which could be made to this work would be to improve the initial models. This could be done either by using a more realistic post-core collapse initial models or updating the code to allow it to follow collapse and bounce itself, similar to H\"udepohl *et al.* (2010) and Fischer *et al.* (2010). Such improvements will affect the early time evolution, but are probably less important to the evolution of the PNS after one second. Additionally, a more realistic equation of state that includes nuclei at low densities (Shen *et al.* 2011) should be employed with consistent opacities.

Of course, this work has also been limited to one dimension, which may be a gross, although necessary, oversimplification. Convection, magnetic fields, and rotation

may be central players in the evolution of PNSs. Approximate mixing length convection will be included in a subsequent version of the code. In the future, this code will be applied to understanding the diffuse supernova neutrino background, predicting the affects of different prescriptions for the nuclear equation of state on PNS cooling, and investigating black hole formation.

I gratefully acknowledge Sanjay Reddy, Vincenzo Cirigliano, and Gang Shen for useful discussions about this work and for help with the opacities and equation of state used in sections 5 and 6.2. I also thank Stan Woosley for numerous useful discussions concerning this work and for a careful reading of the manuscript. I acknowledge support from the University of California Office of the President (09-IR-07-117968-WOOS) and assistance during the early stages from an NNSA/DOE Stewardship Science Graduate Fellowship (DE-FC52-08NA28752). This research has also been supported at UCSC by the National Science Foundation (AST-0909129).

APPENDIX CODE TESTS

Here I consider static transport through an homogeneous sphere with unit radius, and unit optical depth. A flat space-time is assumed. The first test performed is for consistency between the formal solution of the Boltzmann equation and the moment equations. In addition to the factors g_2 and g_3 , the formal Boltzmann solver can also calculate $g_1 \equiv w^1/w^0$ which should be equal to H_g/E_g . For a purely absorptive atmosphere, the formal solution is exact. A comparison of g_1 and H_g/E_g is shown in figure 10. For this calculation, one hundred equally spaced radially zones and a grid of 150 tangent rays with impact parameters spaced equally in radius were used. The calculation was then evolved for ten units of time. The differences between the two Eddington factors are negligible, aside from in the inner most zones. This agreement does not depend strongly on the number of tangent rays employed. The disagreement in the inner most regions is due to the small number of tangent rays which have impact parameters that

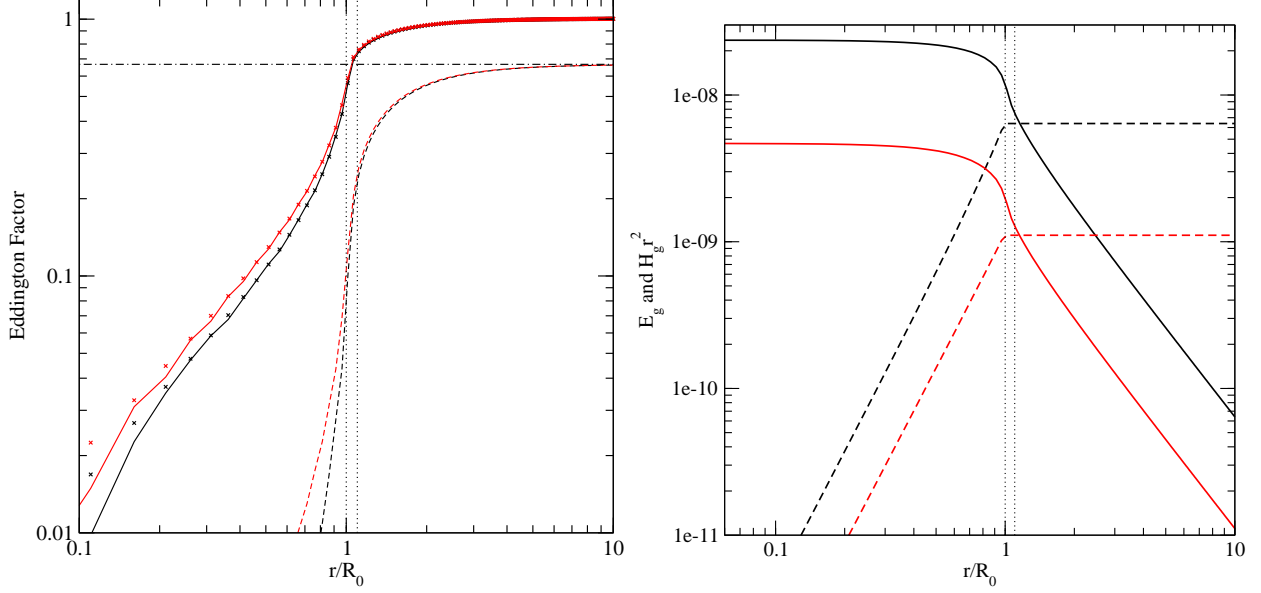


Figure 11. Top Panel: Eddington factors for radiation streaming from a homogenous sphere into free space. The solid lines are the Eddington factors g_1 for the purely absorptive sphere (black) and the isotropic scattering sphere (red). The crosses show H_g/E_g . The dashed lines are the second Eddington factor, g_2 , for the same models. The vertical dotted lines show the radii at which the opaque sphere ends. The horizontal dashed line shows the expected asymptotic value of g_2 for free streaming radiation. Bottom Panel: Properties of the radiation field as a function of radius. The solid lines show the radiation energy density and the dashed lines show the luminosity per steradian, $r^2 H_g$. The colors are the same as in the top panel. Once again, the vertical dotted line denotes the end of the opaque sphere.

are less than the radius at which the Eddington factor is calculated. The distribution function is not well resolved and is therefore in error. Such problems should not arise in the actual evolution of PNSs, as the inner most regions are generally opaque.

As a second test, a sphere which includes a scattering contribution to the opacity is considered. In this case, the formal Boltzmann solver no longer gives an exact solution of the transport equation because of the approximate treatment of the scattering terms (see section 3). The problem set up involves a sphere of optical depth one with 10% of the opacity coming from absorption and 90% coming from isotropic scattering. Using a similar numerical set up to the absorbing atmosphere gives the results shown in figure 10. Once again the deviation between the formal solution and the results of the moment calculation are small. Above the two innermost zones, the maximum deviation of the two results for g_1 is less than 1%. At radii greater than 8, the deviation is less than 0.1%. A second scattering test problem was run with the isotropic scattering opacity, χ_0^s , set to zero and the first order scattering opacity, χ_1^s , set to 90% of the total opacity. The sphere was assumed to have an optical depth $\tau = 0.1$. The agreement between the moment calculation and the formal solution was found to be similar to the isotropic scattering case.

Tests similar to the homogeneous sphere tests of Rampp & Janka (2002) have also been performed. In these, a unit optical depth sphere of radius one is included inside a transparent region of radius ten, with a sharp transition region from the semi-opaque sphere to the surrounding vacuum. Such a scenario is similar to the neutrino decoupling region of PNSs, and is therefore an important test problem for any neutrino transport code for PNS evolution. The calculation domain is split up into 200 zones, equally spaced in radius and 301 a grid of 301 tangent is employed. Only the radiation density, E_g and flux, H_g , are evolved. The calculation is then run for fifty time steps, which allows the calculation to relax to steady state and forget the details of the initial conditions of the radiation field. Once again, one calculation was run with a purely absorbing opacity and a second was run with 10% absorbing opacity and 90% isotropic scattering opacity.

The final Eddington factors and radiation field for these calculations are shown in figure 11. For the purely absorbing calculation, the formal solution of the Boltzmann equation is exact. In the inner most zones, the distribution function is under resolved in angle due to the small number of tangent rays which pass through this region. This is not a problem for PNS simulations, as the optical depth in the interior is always much larger than one. Therefore, the Eddington factors are close to zero and have negligible effects on the moment transport solution. The deviation of the moment solution, outside the inner most region, from the formal solution is less than 1%. In the decoupling region the agreement is excellent. Additionally both g_1 and g_2 asymptote to their expected values for free streaming radiation far from the core.

EQUILIBRIUM FLUX LIMITED DIFFUSION

In the diffusion approximation, the distribution function is approximated by $f(\omega, \mu) = f_0(\omega) + f_1(\omega)\mu$. This results in $g_2 = g_3 = 0$. The time dependence is then dropped and compression terms are then dropped from the first moment equation. Ignoring the terms containing derivatives with respect to energy (which will drop out in the end of our

analysis anyway), I find

$$\Gamma \left(\frac{\partial w^0}{\partial r} + 4 \frac{\partial \phi}{\partial r} w^0 \right) = 3s^1 \quad (\text{B1})$$

If the redshifted frequency is denoted as $\nu = \omega e^\phi$, the redshifted source function is

$$s^1 = -w_1 D^{-1}(\nu e^{-\phi}) \quad (\text{B2})$$

which gives the redshifted neutrino flux per energy

$$w_1 = -\Gamma \frac{D(\nu e^{-\phi})}{3} \left(\frac{\partial w^0}{\partial r} + 4 \frac{\partial \phi}{\partial r} w^0 \right) \quad (\text{B3})$$

where $D(\omega) = (1/\lambda_a^* + \chi_0^s - \chi_1^s/3)^{-1}$. This amounts to assuming that the neutrino flux instantaneously equilibrates to the gradients in the neutrino number density. Because a number of terms have been dropped, this expression does not guarantee that $w_1 \leq w_0$, which means that it is possible for the neutrino fluxes to violate causality (Levermore & Pomraning 1981). This problem is usually circumvented by introducing a flux limiter, which is a correction to the diffusion coefficient which depends on $\xi = w_1/w_0$ and serves to keep the fluxes causal. In section 6.1, the flux limiter of Levermore & Pomraning (1981) has been used, but it was found in Pons *et al.* (1999) that the results of EFLD calculations are reasonably insensitive to the choice of flux limiter.

The total energy flux is given by

$$H = \int d\omega w^1 = -e^\phi \Gamma \int d\omega \frac{D(\nu e^{-\phi})}{3} \left[\frac{\partial w^0}{\partial r} - e^{4\phi} \frac{\partial e^{-4\phi}}{\partial r} w^0 \right] \quad (\text{B4})$$

The equilibrium portion of the EFLD approximation constitutes assuming that $f_0(\omega) = f_{\text{eq}}(\omega, T, \mu)$. Using the equilibrium expression for w_0 yields

$$H = -\frac{\Gamma}{6\pi^2} \int d\omega D(\omega) \omega^3 \frac{\partial f_{\text{eq}}(\omega)}{\partial r} \quad (\text{B5})$$

The radial derivative is then given by

$$\frac{\partial f_{\text{eq}}(\nu e^{-\phi})}{\partial r} = \left[\frac{\omega}{T} \frac{\partial T e^\phi}{\partial r} + T e^\phi \frac{\partial \eta}{\partial r} \right] \frac{f_{\text{eq}}(\omega)(1 - f_{\text{eq}}(\omega))}{T e^\phi} \quad (\text{B6})$$

So that the energy flux is given by

$$H = -\frac{\Gamma e^{-\phi} T^3}{6\pi^2} \left[D_4 \frac{\partial T e^\phi}{\partial r} + D_3 T e^\phi \frac{\partial \eta}{\partial r} \right], \quad (\text{B7})$$

where the energy integrated diffusion coefficients are defined as

$$D_n = \int_0^\infty dx x^n D(xT) f_{\text{eq}}(xT) (1 - f_{\text{eq}}(xT)). \quad (\text{B8})$$

The number flux equation can easily be determined from the energy flux equation. This gives

$$F = -\frac{\Gamma e^{-\phi} T^2}{6\pi^2} \left[D_3 \frac{\partial T e^\phi}{\partial r} + D_2 T e^\phi \frac{\partial \eta}{\partial r} \right]. \quad (\text{B9})$$

These expressions agree with the results of Pons *et al.* (1999).

Now all that is left is to describe the evolution of the underlying medium. Using equation 32, the evolution of the total internal energy of the medium including neutrinos is found to be

$$\frac{\partial \epsilon}{\partial t} + e^\phi \Theta \frac{p}{n} + e^{-\phi} \frac{\partial}{\partial a} \left(\sum_{\{\nu_e, \dots\}} 4\pi r^2 e^{2\phi} H_s \right) = 0 \quad (\text{B10})$$

Using equation 33, the evolution of total lepton number is found to be

$$\frac{\partial Y_L}{\partial t} + \frac{\partial}{\partial a} (4\pi r^2 e^\phi [F_{\nu_e} - F_{\bar{\nu}_e}]) = 0. \quad (\text{B11})$$

REFERENCES

- Anderson, E., et al. 1999, LAPACK Users' Guide, 3rd edn. (Philadelphia, PA: Society for Industrial and Applied Mathematics)
Ando, S. 2004, ApJ, 607, 20
Bionta *et al.*, R. M. 1987, Physi. Rev. Lett., 58, 1494
Bruenn, S. W. 1985, ApJS, 58, 771
Buras, R., Rampp, M., Janka, H.-T., & Kifonidis, K. 2006, A&A, 447, 1049
Burrows, A., & Lattimer, J. M. 1986, ApJ, 307, 178
Burrows, A., Reddy, S., & Thompson, T. A. 2006, Nuclear Physics A, 777, 356
Burrows, A., & Sawyer, R. F. 1999, Phys. Rev. C, 59, 510

- Burrows, A., Young, T., Pinto, P., Eastman, R., & Thompson, T. A. 2000, *ApJ*, 539, 865
- Duan, H., Fuller, G. M., Carlson, J., & Qian, Y.-Z. 2006, *Phys. Rev. D*, 74, 105014
- Ensmann, L. 1994, *ApJ*, 424, 275
- Fattoyev *et al.*, F. J. 2010, *Phys. Rev. C*, 82, 055803
- Fischer, T., Martínez-Pinedo, G., Hempel, M., & Liebendörfer, M. 2011, *ArXiv e-prints*
- Fischer *et al.*, T. 2010, *A&A*, 517, A80+
- Fröhlich, C., Martínez-Pinedo, G., Liebendörfer, M., Thielemann, F.-K., Bravo, E., Hix, W. R., Langanke, K., & Zinner, N. T. 2006, *Physical Review Letters*, 96, 142502
- Fuller, G. M., & Meyer, B. S. 1995, *ApJ*, 453, 792
- Glendenning, N. K., & Moszkowski, S. A. 1991, *Phys. Rev. Lett.*, 67, 2414
- Hannestad, S., & Raffelt, G. 1998, *ApJ*, 507, 339
- Heger, A., Kolbe, E., Haxton, W. C., Langanke, K., Martínez-Pinedo, G., & Woosley, S. E. 2005, *Physics Letters B*, 606, 258
- Hirata *et al.*, K. 1987, *Phys. Rev. Lett.*, 58, 1490
- Horiuchi, S., Beacom, J. F., & Dwek, E. 2009, *Phys. Rev. D*, 79, 083013
- Horowitz, C. J. 2002, *Phys. Rev. D*, 65, 043001
- Horowitz, C. J., & Pérez-García, M. A. 2003, *Phys. Rev. C*, 68, 025803
- Hubeny, I., & Burrows, A. 2007, *ApJ*, 659, 1458
- Hüdepohl *et al.*, L. 2010, *Phys. Rev. Lett.*, 104, 251101
- Janka, H.-T., & Hillebrandt, W. 1989, *A&AS*, 78, 375
- Janka, H.-T., Langanke, K., Marek, A., Martínez-Pinedo, G., & Müller, B. 2007, *Phys. Rep.*, 442, 38
- Keil, M. T., Raffelt, G. G., & Janka, H.-T. 2003, *ApJ*, 590, 971
- Keil, W., & Janka, H.-T. 1995, *A&A*, 296, 145
- Keil, W., Janka, H.-T., & Raffelt, G. 1995, *Phys. Rev. D*, 51, 6635
- Keil, W., Janka, H.-T., Schramm, D. N., Sigl, G., Turner, M. S., & Ellis, J. 1997, *Phys. Rev. D*, 56, 2419
- Kiziltan, B., Kottas, A., & Thorsett, S. E. 2010, *ArXiv e-prints*
- Lattimer, J. M., & Yahil, A. 1989, *ApJ*, 340, 426
- Levermore, C. D., & Pomraning, G. C. 1981, *ApJ*, 248, 321
- Liebendörfer, M., Messer, O. E. B., Mezzacappa, A., Bruenn, S. W., Cardall, C. Y., & Thielemann, F.-K. 2004, *ApJS*, 150, 263
- Liebendörfer, M., Mezzacappa, A., & Thielemann, F.-K. 2001a, *Phys. Rev. D*, 63, 104003
- Liebendörfer, M., Mezzacappa, A., Thielemann, F.-K., Messer, O. E., Hix, W. R., & Bruenn, S. W. 2001b, *Phys. Rev. D*, 63, 103004
- Liebendörfer, M., Rampp, M., Janka, H.-T., & Mezzacappa, A. 2005, *ApJ*, 620, 840
- Lindquist, R. W. 1966, *Ann. of Phys.*, 37, 487
- Loredo, T. J., & Lamb, D. Q. 2002, *Phys. Rev. D*, 65, 063002
- Mayle, R., Wilson, J. R., & Schramm, D. N. 1987, *ApJ*, 318, 288
- Messer, O. E. B., Mezzacappa, A., Bruenn, S. W., & Guidry, M. W. 1998, *ApJ*, 507, 353
- Mezzacappa, A., & Bruenn, S. W. 1993, *ApJ*, 410, 740
- Mezzacappa, A., & Messer, O. E. B. 1999, *Journal of Computational and Applied Mathematics*, 109, 281
- Mihalas, D., & Mihalas, B. W. 1984, *Foundations of radiation hydrodynamics*, ed. Mihalas, D. & Mihalas, B. W.
- Misner, C. W., & Sharp, D. H. 1964, *Physical Review*, 136, 571
- Oppenheimer, J. R., & Volkoff, G. M. 1939, *Physical Review*, 55, 374
- Pons, J. A., Ibáñez, J. M., & Miralles, J. A. 2000, *MNRAS*, 317, 550
- Pons, J. A., Miralles, J. A., & Ibanez, J. M. A. 1998, *A&AS*, 129, 343
- Pons *et al.*, J. A. 2001a, *ApJ*, 553, 382
- , 2001b, *Phys. Rev. Lett.*, 86, 5223
- Pons *et al.*, J. A. 1999, *ApJ*, 513, 780
- Press, W. H., Teukolsky, S. A., Vetterling, W. T., & Flannery, B. P. 1992, *Numerical recipes in FORTRAN. The art of scientific computing*, ed. Press, W. H., Teukolsky, S. A., Vetterling, W. T., & Flannery, B. P.
- Pruet, J., Hoffman, R. D., Woosley, S. E., Janka, H.-T., & Buras, R. 2006, *ApJ*, 644, 1028
- Qian, Y.-Z., & Woosley, S. E. 1996, *ApJ*, 471, 331
- Rampp, M., & Janka, H.-T. 2002, *A&A*, 396, 361
- Reddy, S., Prakash, M., & Lattimer, J. M. 1998, *Phys. Rev. D*, 58, 013009
- Reddy *et al.*, S. 1999, *Phys. Rev. C*, 59, 2888
- Roberts, L. F., Shen, G., Cirigliano, V., Pons, J. A., Reddy, S., & Woosley, S. E. 2012, *Phys. Rev. Lett.*, 108, 061103
- Roberts, L. F., Woosley, S. E., & Hoffman, R. D. 2010, *ApJ*, 722, 954
- Schinder, P. J., & Bludman, S. A. 1989, *ApJ*, 346, 350
- Shen, G., Horowitz, C. J., & Teige, S. 2011, *Phys. Rev. C*, 83, 035802
- Sumiyoshi, K., Suzuki, H., & Toki, H. 1995, *A&A*, 303, 475
- Suzuki, T., Nagataki, S., & Wanajo, S. 2006, in *International Symposium on Nuclear Astrophysics - Nuclei in the Cosmos*
- Swesty, F. 1996, *Journal of Computational Physics*, 127, 118
- Thompson, T. A., Burrows, A., & Pinto, P. A. 2003, *ApJ*, 592, 434
- Thorne, K. S. 1981, *MNRAS*, 194, 439
- Timmes, F. X., & Swesty, F. D. 2000, *ApJS*, 126, 501
- Weaver, T. A., Zimmerman, G. B., & Woosley, S. E. 1978, *ApJ*, 225, 1021
- Wilson, J. R., & Mayle, R. W. 1993, *Phys. Rep.*, 227, 97
- Woosley, S. E., Hartmann, D. H., Hoffman, R. D., & Haxton, W. C. 1990, *ApJ*, 356, 272
- Woosley, S. E., Wilson, J. R., Mathews, G. J., Hoffman, R. D., & Meyer, B. S. 1994, *ApJ*, 433, 229
- Woosley, S. E., Wilson, J. R., & Mayle, R. 1986, *ApJ*, 302, 19
- Yueh, W. R., & Buchler, J. R. 1977, *ApJ*, 217, 565